ANALYSIS OF SURROGATE POST-DETONATION URBAN DEBRIS (SPUD) GAMMA RAYS AND SELF-ATTENUATION

A Thesis
Presented to
The Academic Faculty

by

Nathan L Kane

In Partial Fulfillment
of the Requirements for the Degree
Master of Science in
Nuclear Engineering

Georgia Institute of Technology
May 2019

ANALYSIS OF SURROGATE POST-DETONATION URBAN DEBRIS (SPUD) GAMMA RAYS AND SELF-ATTENUATION

Approved by:

Dr. Steven Biegalski Advisor
School of Mechanical Engineering
Georgia Institute of Technology

Dr. C K Wang
School of Mechanical Engineering
Georgia Institute of Technology

Dr. Ken Dayman
Oak Ridge National Laboratory

Date Approved: April 18th 2019

DEDICATION

This thesis is dedicated my parents, Mike and Teresa Kane, who have been incredibly supportive throughout my life.

ACKNOWLEDGEMENTS

I would like to thank my advisor, Dr. Steven Biegalski for his patience, knowledge, and willingness to teach. Without his help, I would not have been able to complete this project. I would like to thank my collaborators; Dr. Ken Dayman, Dr. Tracy Tipping, and Dr. Jacqueline Mann for their work with this project. I would also like to thank my fellow NRE graduate students at Georgia Tech, whose teamwork and comradery have helped me succeed and enjoy myself in graduate school.

This work was made possible by funding from the Defense Threat Reduction Agency under award number HDTRA1-16-1-0037.

TABLE OF CONTENTS

LIST OF TABLES

LIST OF FIGURES

SUMMARY

Despite the importance of post-detonation nuclear forensics, there is a dearth of Standard Reference Materials (SRMs) suitable for such measurements that are traceable back to a national standard. Accordingly, the nuclear forensics community has requested SRMs be produced that mimic the post-detonation fallout debris that includes actinides, urban materials, fission products, and activation products. The National Institute of Standards in Technology (NIST) in concert with partner labs (Federal Bureau of Investigation (FBI) and National Physics Laboratory (NPL)) and with support from the FBI have developed two Surrogate Post-Detonation Urban Debris (SPUD) SRMs to mimic the debris of a city after an Improvised Nuclear Device (IND) detonation. NIST SPUD samples were irradiated at the University of Texas at Austin TRIGA reactor, then analyzed via gamma-ray spectroscopy for short-lived, medium-lived and long-lived fission and activation products. Upon completion of gamma-ray analysis, a self-attenuation analysis used to model the efficiency of a High-Purity Germanium detector (HPGe) as a function of source density and volume was conducted using MCNP.

CHAPTER 1: INTRODUCTION

1.1 Discovery of Nuclear Fission

In attempt to create atoms bigger than uranium, Enrico Fermi starting bombarding uranium with neutrons in 1934. The conventional wisdom at the time was that the neutron would only cause a small change in the number of neutrons or protons in an atom (Tretkoff). Austrian Physicist Lise Meitner and Chemist Otto Hahn followed Fermi's work and starting bombarding uranium with neutrons as well, while identifying the decay products. In December 1938 Hahn appeared to find isotopes of Barium among the decay products and he couldn't explain it. Lise Meitner went back to the liquid drop model and came to the idea that the drop could be elongated and pinched in the middle to form two smaller elements. Meitner also determined that the daughter nuclei together would be slightly less massive than the original uranium nuclei corresponding to a release of about 200 MeV (Tretkoff).

It was soon discovered that the fission reaction also emitted neutrons and therefore a chain reaction was possible. As it being around the time of World War II many scientists all over the world attempted and ultimately succeeded in creating an atomic bomb. Now, many years later, some countries have nuclear arsenals (Russia, China, United States, France, India, Israel, North Korea and the UK) and other countries and some extremist groups are likely attempting to develop atomic bombs as well. Along with strong preventative measures such as diplomacy, surveillance, and radioactive Nobel gas detection, it is imperative to be prepared for the possibility of detonation as well.

1.2 Importance of Nuclear Forensics

Leaders of the United States have agreed for decades that nuclear terrorism is one of the most severe threats to our national security. Not only is there an unimaginable loss of life if an Improvised Nuclear Device (IND) is detonated in a U.S. city, the potential for more detonations could change the way the country operates, putting an increasing amount of resources into national security at the behest of justice, freedom, and general welfare that this country was founded on (National Research Council).

Our ability to perform forensic analyses of nuclear materials, nuclear explosions, and debris can play an integral role toward the deterrence, reduction and response to nuclear terrorism. When working in concert with enhanced efforts to secure nuclear materials, and detect theft and clandestine production of nuclear materials, swift and competent forensics can substantially reduce the threat of nuclear detonation (National Research Council). As U.S. allies will likely fear an attack as well, the ability to exclude allies as a possible origin can allow for their assistance in the analysis and response.

If there is an act of nuclear terrorism on U.S. soil, the president will demand answers to a multitude of questions. What is it? Where did it come from and whose is it? Who had it and how did they get it? Did they have help? Is there more of it out there? What should we do about it? In order to answer these questions their needs to be a method to analyze the signals and debris from the detonation and simulate materials production and weapons performance (National Research Council). Analysis such as time since last separation and trace-constituent are significant as well. This myriad of analyses can provide information on how, when, and potentially where the IND

was made, and design features of the device along with its construction and performance information (National Research Council).

1.3 Nuclear Forensics Studies

In order to discover more about nuclear detonation, from fall 1961 to summer 1962 a series of 44 underground nuclear tests, referred to as Operation Nougat, was conducted (DOE 2015). Tunnels and vents were designed to limit radiation exposure to populated areas (USPHS). On April 14th, 1962 the Platte test was performed at the Nevada Test Site, now known as the Nevada National Security Site. A 1.6kT Pu-239 bomb was triggered underground and the radioactivity was measured. The radioactivity was measured in Area A and Area B one week after detonation, and again two years after detonation. Area A is located close to the test location, and Area B is 63km 20 degrees east of north in Queen City Summit (Burnett and Milbrath). The radiation from the explosion two years later could only be measured in Area A.

The United States had many operations similar to Operation Nougat in the 1960s where various nuclear explosions were tested. The analysis of these tests provided an understanding of nuclear weapons design and performance that allows US strategic Command to verify the safety and reliability of US nuclear weapons stockpiles without further nuclear testing. Although this analysis is useful in nuclear forensics, the ability to quickly and accurately analyzing unknown materials and detonation debris is much more difficult than characterizing the radiation released from a known device (National Research Council).

The fact remains that there is no standard reference material (SRM) in which the debris could be compared to. This work involves neutron activation and gamma ray analysis of Surrogate Post-

detonation Urban Debris (SPUD) samples in attempt to develop a standard method for identifying the composition of an IND from its post-detonation debris.

There are many factors that contribute to the efficiency of a detector. Additionally, it is very important to have an accurate knowledge of detector efficiency when analyzing the contents of complex samples. Samples can be cut to the same size to keep the source-detector geometry constant. However, reducing the size of a debris sample will reduce the activity, and if it is already a low activity source, it can be hard to detect with low uncertainty, especially for short-lived isotopes because a longer count time will be ineffective in its attempt to increase counts. Furthermore, the density of the material in the sample also plays a factor in the detector efficiency and it is not as easy to normalize. The attenuation of gamma rays within the sample itself, is referred to as self-attenuation, or self-shielding and it depends on material density and atomic number (z). Self-shielding effects the detector efficiency and as such it is necessary to develop a process to calculate the efficiency of the detector as a function of material density.

1.4 Self-Shielding

It is of the utmost importance to be as precise as possible in post-detonation gamma ray analysis and one of the biggest problems contributing to accuracy is self-attenuation of the gamma rays. Self-shielding tends to appear more as samples increase in size and density, especially for low energy photons. There is a common process for calculating attenuation known as the transmission-technique or T-technique. In this case, large (or good) geometry is needed. That means the source and detector are so far away that the source size can be essentially neglected and treated as a point. This allows for a sheet of some attenuator material (i.e. Lead) to be placed between the source and the detector to see what percentage of photons are attenuated. This is

referred to as linear attenuation, and the linear attenuation coefficient of many materials are well documented. Cutshall et al. attempted to derive an equation to essentially convert the linear attenuation coefficient of a material to a self-attenuation equation for cylindrical samples (Cutshall). However, many authors have questioned the method claiming it causes systematic errors (Jodlowski).

This work uses Monte Carlo methods to determine the absolute efficiency of a detector given source-detector geometry and source density.

1.5 Monte Carlo Methods

Rather than classical deterministic transport, Monte Carlo methods model radiation transport stochastically. Specifically, Monte Carlo N-Particle transport code (MCNP) was used in this work. MCNP is a versatile code; the user can model various geometries, interactions and even different types of radiation (i.e. Photons, neutrons and electrons). MCNP6.1 was used for the simulations in this work.

1.6 Statement of Goals

The goals of this work are as follows:

1. To accurately analyze the contents of the SPUD samples.
2. To create a model that describes the efficiency of a detector given the material density and photopeak energy.
3. To create an algorithm to determine detector efficiency given the ratio of the efficiency at two or more different energies.

CHAPTER 2: THEORY

2.1 Gamma Decay

Gamma radiation is a form of electromagnetic radiation; a photon of high energy. It occurs when the nucleus is in an unstable or excited state. For the examples most relevant to this work; activation and fission products have too many neutrons to be stable, so they first go through beta-minus decay to change a neutron into a proton. The resulting nucleus is still unstable, so it then emits a gamma-ray to lower its energy and reach ground state.

2.2 Gamma Interactions with matter

The are many mechanisms in which gamma-rays can interact with matter but the three most prevalent are photoelectric absorption, Compton scattering, and pair production. In these interactions there is either full or partial energy transfer from the incoming gamma ray to an atomic electron of the absorber. Full energy transfer results in the disappearance of the photon, while partial energy transfer changes the direction of the photon.

2.2.1 Photoelectric Absorption

Photoelectric absorption, which typically occurs for low energy photons, results in full energy transfer from the photon to the atomic electron. Once the electron is ejected from the atom, it needs to be replaced. The electron can be replaced by either a transfer of an electron from another shell, or the absorption of a foreign electron. In the case of an electron from a different energy level moving to the shell in which the initial electron was ejected, characteristic X-rays are released. These can be reabsorbed to produce Auger Electrons by either the atom that emitted the X-ray, or a neighboring atom (Knoll). The figure below illustrates photoelectric absorption.

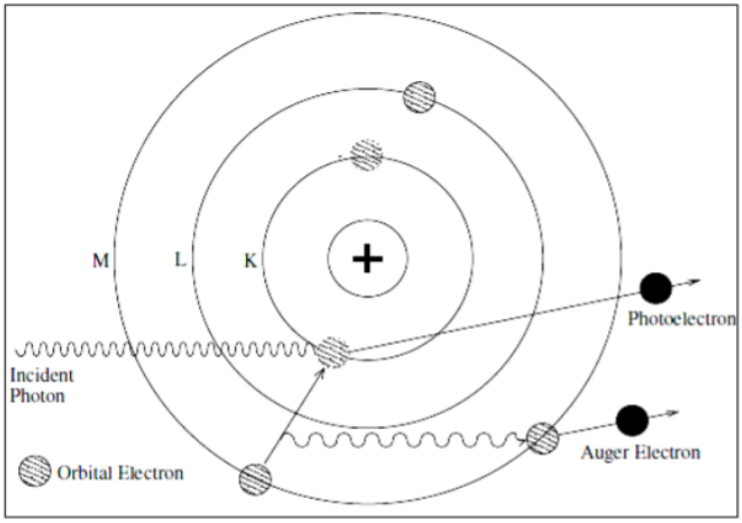

Figure 1: Photoelectric Effect

The energy of the resulting electron is given in Equation 2.1

$$E_e = E_\gamma - B_e \tag{2.1}$$

Where E_γ is the energy of the incident photon, and B_e is the binding energy of the electron to the atom. The binding energy tends to be negligible as it is on the order of eV and the photon energy can be anywhere from 10keV to a few MeV.

2.2.2 Compton Scattering

Compton scattering results in a partial transfer of energy from the photon to the electron, and a (typically large) change of direction of the photon.

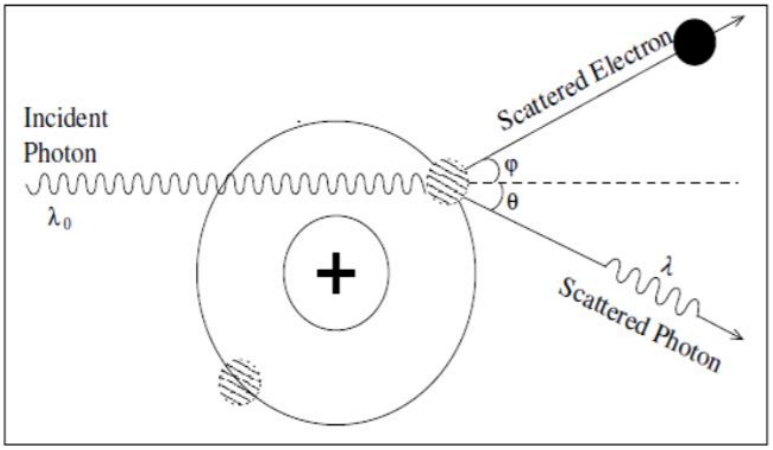

Figure 2: Compton Scattering (Abdullah)

The energy of the new photon, hv', is always less than that of the incident photon and is characterized in Equations 2.2 and 2.3 (Knoll).

$$E_{\gamma'} = E_{\gamma} - E_e - B_e \tag{2.2}$$

$$E_{\gamma'} = \frac{E_{\gamma}}{1+\frac{511}{E_{\gamma}}(1-cos\theta)} \tag{2.3}$$

The rest mass energy of an electron is 511 keV, therefore the energy of the photons also needs to be expressed in keV for this equation to remain valid. As apparent in Equation 2.3, the energy of the scattered photon is dependent on θ, the scattering angle of the photon. This leads to a spectrum of energies for the photon, and in turn, the electron.

2.2.3 Pair Production

Pair production refers to the creation of a positron-electron pair during the absorption of the photon. By definition, pair production can only occur for photons above 1022 keV and isn't very common until energies much higher than that. It is similar to photoelectric effect in that there is full energy transfer from the photon. The electron and positron will split the remaining energy equally, as they shoot of into opposite directions in the center of mass system. Figure 2.3 shows a

schematic representation of the pair production process. Also shown in Figure 2.3 is the annihilation reaction of the positron in which it collides with an electron and both particles are annihilated leaving two 511 keV photons in their wake.

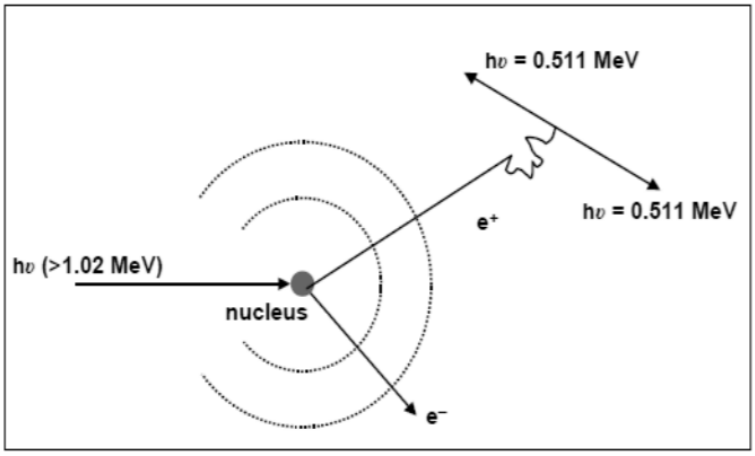

Figure 3: Pair Production (Abdullah)

The electron and positron equally split the remaining energy of the photon as described in Equation 2.4

$$E_- = E_+ = \frac{E_\gamma - 1022keV}{2} \tag{2.4}$$

All of these photon-electron interactions compete with each other. Figure 2.4, affectionately known as the Volcano Plot, shows the regions where each interaction mechanism is dominant.

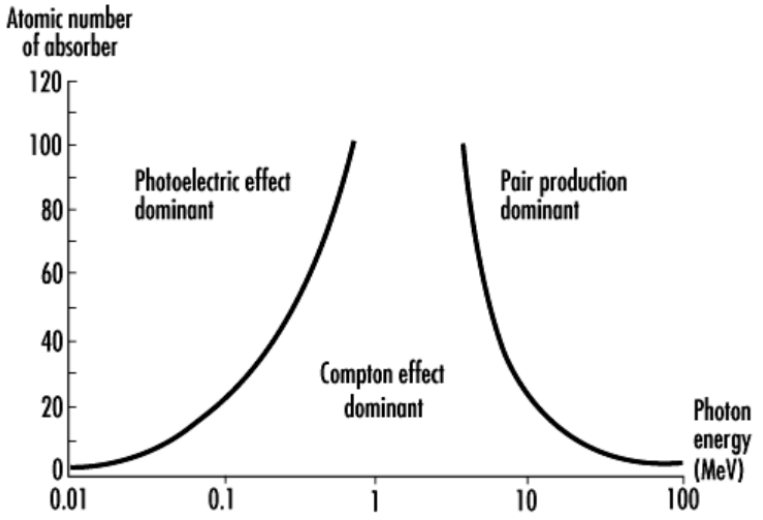

Figure 4: Volcano Plot (Encyclopedia of Occupational Health and Safety 4th Edition)

The lines correspond to where the probability of Compton scattering is equal to the probability of adjacent interaction mechanism.

2.3 Photon Interactions and Self-Shielding

Self-shielding occurs when a photon undergoes one of the aforementioned photon interactions with the source itself. The ensuing figure shows provides a representation of self-attenuation of the photons via the photoelectric effect.

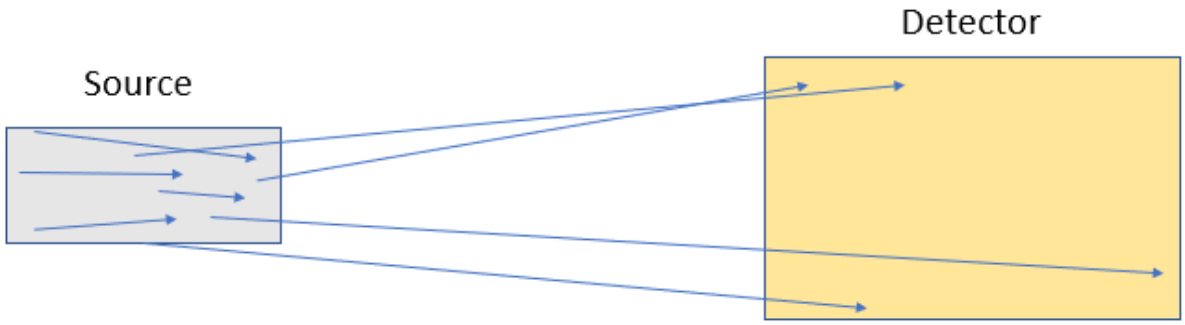

Figure 5: Self-Shielding via Photoelectric Effect

The arrow tail represents the start of the photons trajectory and the head represents the end of it. In this case, some photons fully absorb in the sample itself resulting in a lower efficiency in the detector. If Compton scattering occurs within the sample, there are three possible effects:

1. The photon was traveling in the direction of the detector and the scatter caused it to miss the detector.
2. The photon was traveling in the direction of the detector and the scatter resulted in a lower energy photon reaching the detector.
3. The photon on track to miss the detector, but the scatter caused it to land in the detector.

This will cause two effects; a loss of peak efficiency from the photons missing the detector, and a larger Compton edge from the lower energy photons reaching the detector. The following figures physically represent Compton scattering within the sample.

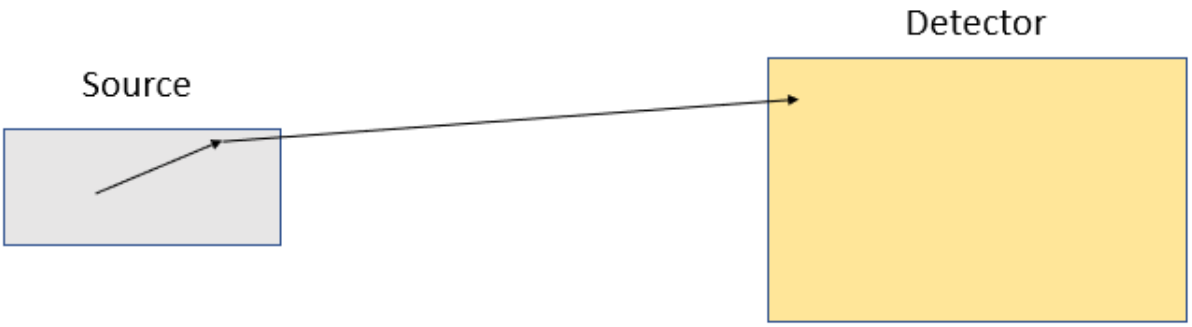

Figure 6: Compton Scattering 1

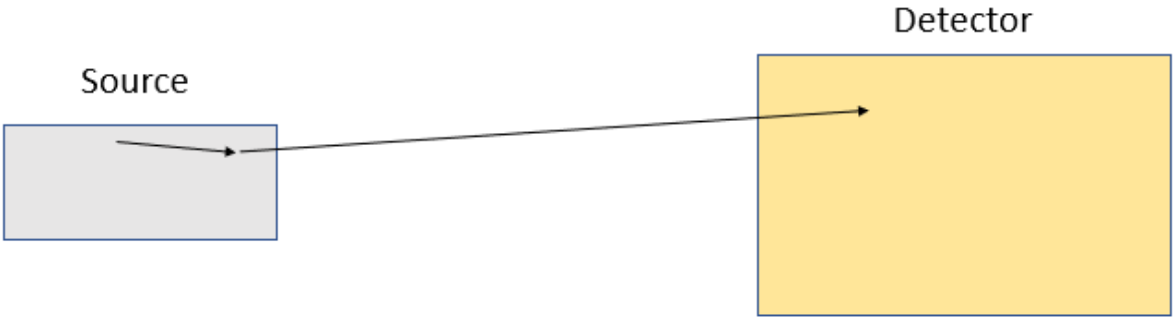

Figure 7 Compton Scattering 2

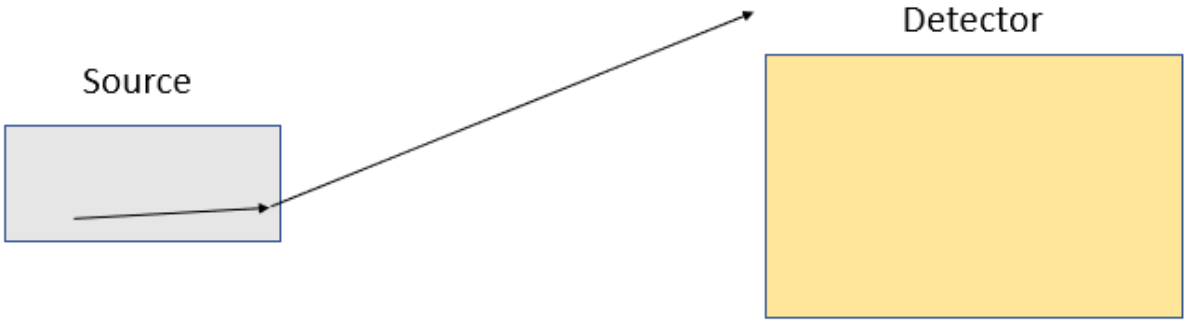

Figure 8: Compton Scattering 3

Finally, after pair production occurs, the electron will deposit its energy in the source, and the position will undergo an annihilation reaction. Some of the 511 keV photon from said reaction will reach the detector and contribute to the annihilation peak.

2.4 High Purity Germanium Detectors (HPGe)

The function of any radiation detector is to convert the incoming radiation into a signal that can be observed, typically in either the form of an electric current or a voltage pulse. Germanium is semiconductor, so it goes about generating the current differently than most detectors. Semiconductors have a valence band and a conduction band separated by what is referred to as the band gap as shown in Figure 5. The band gap of germanium is only about .7eV which results in too much thermal excitation of electrons across the band gap at room temperature, and the leakage current would be too high (Knoll). This is combatted by using liquid nitrogen to cool the HPGe to an operating temperature of 77 Kelvin. Despite the cost and inconvenience of cooling the HPGe, its low band gap is imperative to its high energy resolution. The low band gap allows the energy per electron-hole pair, w, to be about 3 eV. This is much smaller than the w value of typical gas filled detectors which range from about 26 eV to 40 eV (Knoll). The smaller w value allows for the creation of more charge carriers, n, for a given energy deposition as shown in the equation below, where E is the energy deposition of the incident radiation.

$$n = \frac{E}{w} \tag{2.5}$$

The resolution is a measure of statistical uncertainty, and as such it is proportional to $n^{-1/2}$.

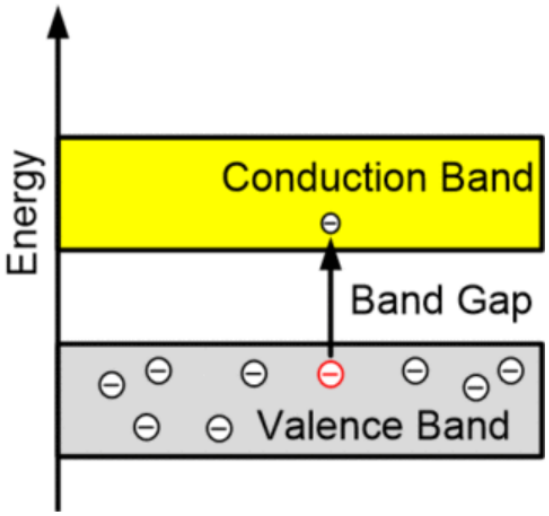

Figure 9: Semiconductor Band Gap (Faizan)

In pure semiconductors, such as Figure 9 the conduction band is empty, so if an electron can cross it, then it can move freely within the conduction band. Detectors are doped with impurities referred to as n-type and p-type. It is impossible to get completely pure germanium, but the impurity concentration can be as low as $2.4\text{x}10^{13}$ cm^{-3}(Knoll). N-type impurities are elements of group five on the periodic table because they have an extra electron they are looking to donate; hence the name, donor impurities. P-type impurities are group three elements and are referred to as acceptor impurities because they are an electron short and therefore will accept electrons. In an HPGe, one side of the germanium is n-type while the other is p-type making the middle a p-n junction. Gaseous diffusion of lithium is used to allow the n and p-type germanium to come together, which then triggers a small diffusion of electrons from the n-type to the p-type (Knoll). This creates a region in the middle of the HPGe that is neither n-type or p-type and is referred to as the depletion region because the free charges are depleted. The thickness (or depth) of the depletion region is given by the following equation (Knoll).

$$d = \left(\frac{2\epsilon V}{eN}\right)^{1/2} \tag{2.6}$$

Where d is depth, ϵ is the dielectric constant, V is the reverse bias voltage, N is the net impurity concentration, and e is the electronic charge. It is necessary to make this region as large as possible to be effective in gamma spectroscopy in order to achieve full energy deposition of the highest percentage of gamma rays possible and reduce the Compton Edge. As apparent from the equation, the higher the applied voltage, the larger the depletion region, however, one must be careful because the increased voltage will also lead to an increased leakage current. Leakage current can render the detector useless if it approaches the magnitude of the current produced from an event in the active volume. That is why high purity germanium is used, because the fewer impurities leads to less leakage current. Once the high purity germanium is produced, the applied voltage is optimized to maximize depletion depth while keeping below a leakage current threshold. This results in an operating voltage of about 3500 volts.

2.5 Detector Electronics

In order for incident radiation to be detected, the detector system must convert the charge deposition of the radiation into either electric current or a voltage pulse. HPGe detectors are operated in pulse mode, meaning the charge deposition is converted into a voltage pulse. The advantage of pulse mode is that the timing and energy characteristics of each deposition can be recorded, whereas in current mode, the average counts per second are recorded (Knoll). The HPGe is connected to a preamplifier as shown in Figure 10.

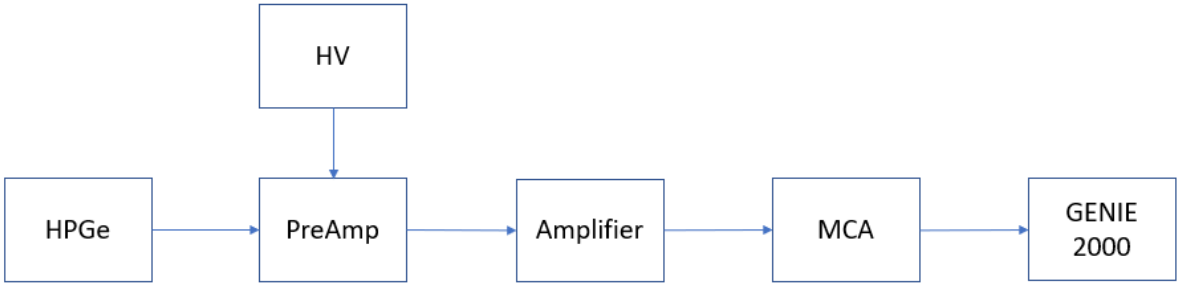

Figure 10: Detector Electronics

The preamp converts electric charge produced by the radiation event into a voltage pulse proportional to the energy deposited. The preamp has a few more functions as well including impedance matching, improving signal to noise ratio, and pulse shaping to limit pulse pileups. Pulse pileup occurs when two pulses are closely spaced in time and, consequently, interfere with each other. Since radioactivity is a stochastic process, there is the possibility for multiple decays to happen in an extremely short time frame, leading to pulse pileup (Knoll). This is especially prevalent in high activity samples. The HV or high voltage supply provides enough voltage for the system to work. The amplifier increases the voltage pulse from the preamp so that it can be detected. The MCA or multi-channel analyzer us used in the case of spectroscopy. The MCA has thousands of channels which correspond to energy bins so that different energy photons can be distinguished because they appear in different energy bins. Finally, GENIE 2000 is used to observe and analyze the spectrum.

2.6 Practical Gamma Spectroscopy

Unfortunately, the spectrum isn't as simple as full energy deposition for all the gamma rays. There are instead a number of peaks that can occur from photons of just one energy as shown in Figure 11.

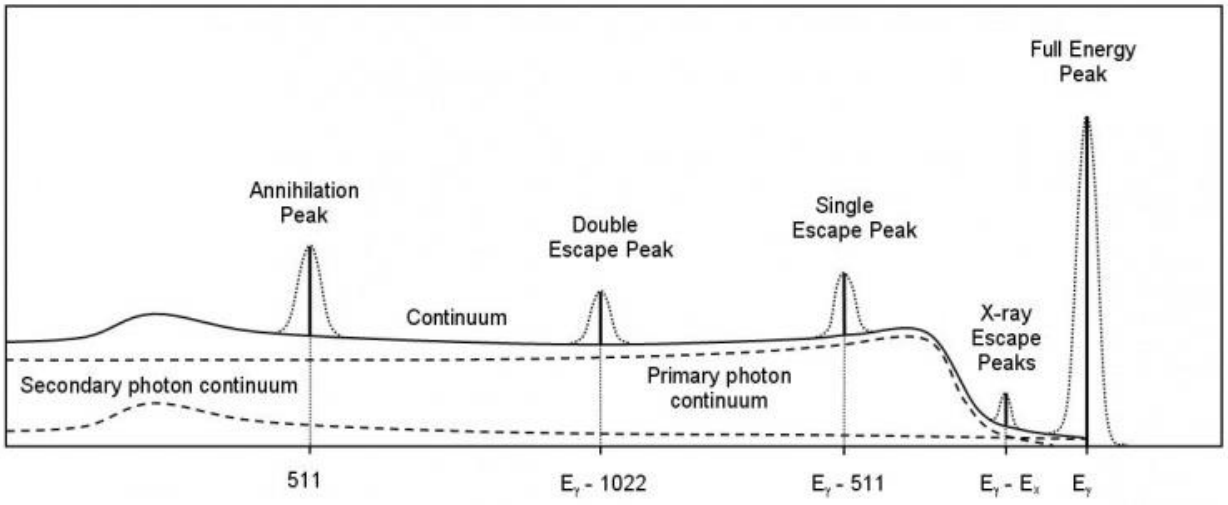

Figure 11: Gamma Spectrum (Berlizov, 2011)

The annihilation peak arises when pair production occurs in material outside the active detector volume. One of the 511 keV photons enters the depletion region and fully deposits to create the annihilation peak. Conversely, the single and double escape peaks are due to pair production inside the depletion region, but one or two of the 511 keV photons leave the depletion region without depositing energy. The Compton Edge is a result of partial energy deposition during Compton Scattering; the electron fully deposits energy in the detector, but the secondary photon escapes. It appears as a continuum because the photons can scatter in many directions resulting in various amounts of energy transfer. Finally, the peak missing from Figure 11 is the sum peak. The sum peak is a result of coincidence summing. Similar to pulse pileup, this occurs when multiple decays to happen in an extremely short time frame. However, in this case rather than two separate pulses, the two photons deposit their full energy in the depletion region within a time window shorter than the resolving time in the detector, and the count appears at the sum of those photon energies hence the name sum peak. In the case of a monoenergetic source such as Figure 11, the sum peak would appear at $2E_\gamma$. Another phenomenon to be aware of during gamma spectroscopy is detector dead time. Dead time is the minimum amount of time it takes for a detector to be able

to distinguish between two pulses (Knoll). Along with pulse pileup, and coincidence summing, dead time effects also increase as source activity increases.

2.7 Monte Carlo Methods and MCNP

There are many ways to model radiation transport. One common way is to use discrete ordinates method, which is a deterministic method. Deterministic methods solve the transport equation for the average particle behavior. It involves splitting the problem into lots of small phase space boxes, and averaging the particle speed, angular dependence, and location (MCNP User Manual, Revised February 2008).

The Monte Carlo method instead simulates individual particles and records mean and standard deviation of the desired feature. The average behavior of the entire system is then deduced from the average behavior of the particles using the central limit theorem (MCNP User Manual). This makes it more effective than the deterministic approach when modeling complex geometries. Monte Carlo methods also benefit from the fact that they only have stochastic uncertainties, whereas deterministic methods have inherent error due to the averaging of particle information over a phase space.

Monte Carlo methods involve the simulating of some number of particle histories via a random number generator. In each particle history, random numbers are generated and used to determine, for example, the scattering angle or energy deposition in a collision as well as the distance between collisions and more. Experimentally derived cross section data is used in order to assign probabilities to events, such as the probability of photon scatter vs photon capture (MCNP User Manual).

MCNP was developed at Las Alamos National Laboratory (LANL) during the 1940s to study the atomic bomb. It has since been continuously updated at LANL and although it's export-controlled, it's distributed through the Radiation Safety Information Computational Center

(RSICC) at Oak Ridge National Laboratory (ORNL). Although neutron transport can be modeled in MCNP, only photons were modelled for this thesis.

For photons, the code accounts for coherent and incoherent scattering, and fluorescent emission after photelectric absorption (MCNP User Manual). In the case of pair production, it accounts for both the electron and the annihilation reaction of the positron with subsequent photon production. Similarly, it tracks the electron movement, as well as the scattered photon during Compton Scattering. Moreover, during electron/positron transport the code models the production of secondary particles such as characteristic X-rays, Auger electrons, and Bremsstrahlung into account as well (MCNP User Manual). Auger electrons compete with characteristic X-rays; rather than the atomic electron moving between electron shells, the auger electron is an atomic electron that starts in the outer shell and gets ejected from the atom as it absorbs the energy of the incoming photon (Knoll). Bremsstrahlung radiation occurs when an electron is accelerating in a medium. As fast electrons slow down due to coulombic interactions, this deceleration causes the release of electromagnetic radiation (Knoll).

2.7.1 Monte Carlo Mathematics

If we assume a time-independent problem with N particle histories starting by sampling the source distribution to determine the photon's initial energy, position, and direction. The distance the particle will travel before a collision is determined stochastically as a function of its mean free path. Once the location and material of the collision is resolved, the cross section data is sampled and photon-electron interaction is decided. If say, Compton Scattering occurs, the distribution of scattering angles is sampled to provide a new direction (and energy) of the photon. Electron transport is also recorded on the electron ejected during the scatter. This process is repeated until the photon is either absorbed or escapes. In the case of photon absorption, the photon particle history is terminated.

The purpose of particle tracking is to calculate the expected (or mean) value of the desired quantity. The estimate of said quantity would be the mean, *X*, of *N* samples as given by Equation 2.6 below (Lewis and Miller).

$$X = \frac{1}{N}\sum_{n=1}^{N} x_n \tag{2.6}$$

Where x_n is some value of the nth particle's history, such as flight distance or scattering angle. The x_n is tallied from each history to calculate *X* at the end. From counting statistics, the uncertainty of the mean decreases as N increases, in most cases it's proportional to $N^{-1/2}$.

There are two function that are integral to Monte Carlo calculations; the probability density function and the cumulative probability distribution. The probability density function, f(x) is defined by the limit as Δx approaches 0 of

$$f(x)\Delta x = P\{x \leq x' \leq x + \Delta x\} \tag{2.7}$$

Meaning $f(x)\Delta x$ is equal to the probability that x' will be between x and $x + \Delta x$. The probability density function is normalized, therefore, if x is exclusively in the range a to b then the following equation holds true.

$$\int_a^b f(x)dx = P\{a \leq x \leq b\} = 1 \tag{2.8}$$

The cumulative probability distribution, $F(x)$ is defined as the probability that the random variable x' will be less than or equal to x, as shown in Equation 2.9 (Lewis and Miller).

$$F(x) = P\{x' \leq x\} \tag{2.9}$$

The cumulative probability distribution relates to the probability density function via Equation 2.10.

$$F(x) = \int_{-\infty}^{x} f(x')dx' \tag{2.10}$$

It's more common to write the relationship in differential form (Lewis and Miller).

$$\frac{dF(x)}{dx} = f(x) \tag{2.11}$$

For the purpose of Monte Carlo calculations, it is necessary to discuss the rules for transformations of random variables. Consider that $y = y(x)$ is a function of random variable *x*. Then, consider that *g(y)dy* is the probability that *y* is between *y* and $y + dy$ and that *f(x)dx* is the probability that *x* is between *x* and $x + dx$. The probability functions g(y) and f(x) then satisfy the equation (Lewis and Miller).

$$g(y) = f(x)\left|\frac{dx}{dy}\right| \tag{2.12}$$

Now, suppose that *y=F(x)*, where *F(x)* is the CDF, and we can rewrite equation 2.12 as 2.13 (Lewis and Miller).

$$g(F) = f(x)\left|\frac{dx}{dF}\right| = 1 \tag{2.13}$$

This means that F is uniformly distributed between zero and one. Therefore, if F is sampled in an unbiased manner, such as a random number generator, then the sequence of numbers, ξ provided by said generator can be used to sample F(x) in an unbiased manner (Lewis and Miller).

$$F(x) = \xi \tag{2.14}$$

By repeatedly calling the random number generator for values of ξ an unbiased distribution of *F(x)* values is obtained. However, the distribution of *x*, not of *F(x)*, is what is required for Monte Carlo methods. As such, an inversion must be performed as shown in equation 2.15 (Lewis and Miller)

$$x = F(\xi)^{-1} \tag{2.15}$$

The inversion of the CPDs that represent the physical processes (i.e. distance traveled between collisions) is important to the accurate and economic Monte Carlo simulation of particle transport (Lewis and Miller).

2.7.2 Input File

The MCNP input file consists of three parts, referred to as cards, separated by a blank line. The first card is the cell card which contains four pieces of information; the cell number, the material number, the density and location of the cell (MCNP User Manual). The density can either be mass density (g/cc), denoted with a negative sign in front, or number density (atoms/cc). The cell number is typically in ascending order.

The second card is the surface card, and it has three components. Again, each surface is assigned a number typically in ascending order. The second component is the shape of the surface; it contains information about the axis the shape lies on, and whether it's a plain or cylinder. Finally, the size of the surface is noted last (i.e. radius of the cylinder).

The third card is the data card. This is where the mode is denoted (i.e. p for photons). This is also where the tally is determined. Different tallies provide different data, and for this thesis the F8 tally was used because it records the energy distribution of pulses created in a cell that models a physical detector (MCNP User Manual).

This was an extremely brief description of MCNP, for more information the reader is encouraged to read the MCNP User Manual. The source-detector setup that was modelled in this thesis is shown in Figure 12.

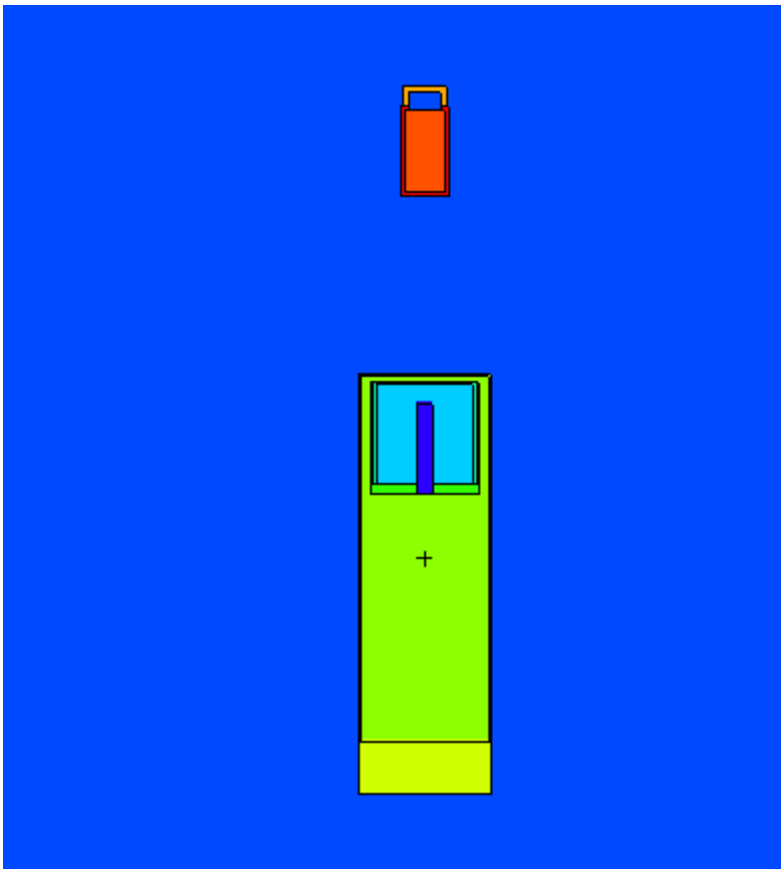

Figure 12: Physical Representation of MCNP Input File

Figure 12 is a side view of the source-detector set up. As such the detector and source appear as rectangles instead of cylinders. In Figure 12 the red cylinder on top is the source and the dark blue in the middle is the germanium.

CHAPTER 3: GAMMA RAY ANALYSIS OF SPUD SAMPLES

3.1 Problem Statement

NIST developed SPUD samples to simulate the fallout from a nuclear explosion. They are samples created with a variety of materials typically found in a city all put together with uranium. There were two types of samples created, the SRM 4600 which used natural uranium, and the SRM 4601 which used uranium enriched to 22% U-235. The uranium was enriched to 22% because it gets difficult to ship in the United States above 22% due to various state and federal laws.

3.2 Experimental Setup

When a nuclear device detonates there are incredibly high fluxes of fast neutrons that will transport into surrounding material resulting in radioactive isotopes due to neutron capture; these are referred to as neutron activation products. The neutrons will also be captured by U-235 or some other fissile isotope and fission creating massive amounts of energy, more neutrons, and radioactive fission products. To simulate this, the SRMs were sent to the University of Texas at Austin where they underwent neutron activation in three separate facilities of the TRIGA reactor.

1) The rotary specimen rack (RSR) is used to support neutron activation analysis and isotope production. The RSR consists of an air-filled water-tight canister enclosing a sample rack and pinion drive assembly that rotates around the reactor core. It is utilized for longer thermal neutron irradiations.

2) The thermal pneumatic transit (tPNT) system takes up one fuel element position in the outer ring of the TRIGA core. This system is used for shorter irradiations on the order of 10 seconds to 2 minutes.

3) The three-element irradiator (3-EL) is a sealed in-core canister that displaces three fuel elements. For these experiments a cadmium lined canister was utilized to remove the thermal neutron component of the spectrum.

Table 1 shows the sample mass, reactor power, corresponding neutron flux, and irradiation time for each of the irradiations. The SRM 4600 and 4601 samples were irradiated simultaneously. Lower sample mass was utilized for the 3-EL irradiations so that samples may be removed and counted a short time after irradiation.

Table 1: Sample Irradiation Conditions

SRM	**Mass (g)**	**Irradiation Facility**	**Power (kW)**	**Flux (cm^{-2} s^{-1})**	**Irradiation Time**
SRM 4600	0.30539	RSR	950	2×10^{12}	1 hour
SRM 4600	0.18909	tPNT	100	3×10^{11}	10 s
SRM 4600	0.05363	3-EL(Cd)	500	5×10^{11} (epithermal)	30 min
SRM 4601	0.25631	RSR	950	2×10^{12}	1 hour
SRM 4601	0.31631	tPNT	100	3×10^{11}	10 s
SRM 4601	0.008084	3-EL(Cd)	500	5×10^{11} (epithermal)	30 min

After irradiation, samples were counted at a distance of 7 cm from an ORTEC HPGe detector shown in Figure 9. Canberra GENIE 2000 gamma-ray spectroscopy software was utilized for spectrum acquisition and analysis. The tPNT, 3-EL(Cd), and RSR irradiations were left to decay for approximately 10 minutes, 2 days, and 2 weeks, respectively prior to gamma-ray acquisition.

Figure 13: ORTEC HPGe detector system utilized for gamma-ray spectroscopy

The GENIE 2000 digitized the spectra with peaks at various energies. The HPGe detector was calibrated for energy, resolution and efficiency using a multi-gamma Standard Reference Source produced by Eckert & Ziegler Analytics shown in Table 2. The source was distributed in a small cylinder, the same geometry as the SPUD samples analyzed in this project.

Table 2: Multi-Gamma Standard

Reference Date: 01-January-2018 12:00 PM EST
MGS Mixture

Isotope	Gamma-Ray Energy, keV	Half-Life, d	Activity, Bq	Flux, s^{-1}	Uncertainty u_A, %	Uncertainty u_B, %	Uncertainty U, %*	Calibration Method**
Pb-210	46.5	8.109E+03	1.450E+04	6.163E+02	0.1	2.1	4.2	4π LS
Am-241	59.5	1.580E+05	1.162E+03	4.172E+02	0.1	1.8	3.6	4π LS
Cd-109	88.0	4.614E+02	1.610E+04	5.955E+02	0.5	2.0	4.1	HPGe
Co-57	122.1	2.717E+02	3.654E+02	3.128E+02	0.4	1.7	3.4	HPGe
Ce-139	165.9	1.376E+02	5.499E+02	4.399E+02	0.4	1.7	3.6	HPGe
Hg-203	279.2	4.659E+01	1.185E+03	9.665E+02	0.3	1.7	3.5	HPGe
Sn-113	391.7	1.151E+02	9.407E+02	6.112E+02	0.4	1.9	3.9	HPGe
Cs-137	661.7	1.099E+04	4.612E+02	3.925E+02	0.7	1.9	4.1	HPGe
Y-88	898.0	1.066E+02	1.577E+03	1.478E+03	0.7	1.7	3.7	HPGe
Y-88	1836.1	———	———	1.565E+03	0.7	1.7	3.7	———
Co-60	1173.2	1.925E+03	7.219E+02	7.208E+02	0.7	1.8	3.9	HPGe
Co-60	1332.5	———	———	7.217E+02	0.7	1.8	3.9	———

3.3 GENIE 2000

The GENIE 2000 software goes through a series of steps; first it finds the location (unidentified second difference method was utilized) and area (sum/nonlinear LSQ fit was utilized) of the peak. Once the library and efficiency calibration file were selected, the activity of each recognized nuclide was calculated. The final step was to perform the parent-daughter correction for nuclides in a decay series. A list of unidentified peaks was also examined for unidentified major gamma-ray lines, which primarily consists of sum peaks and escapes peak. GENIE 2000 isn't very picture-friendly, so Figure 14, which displays the SMR 4601 long-lived spectrum, was made in Excel.

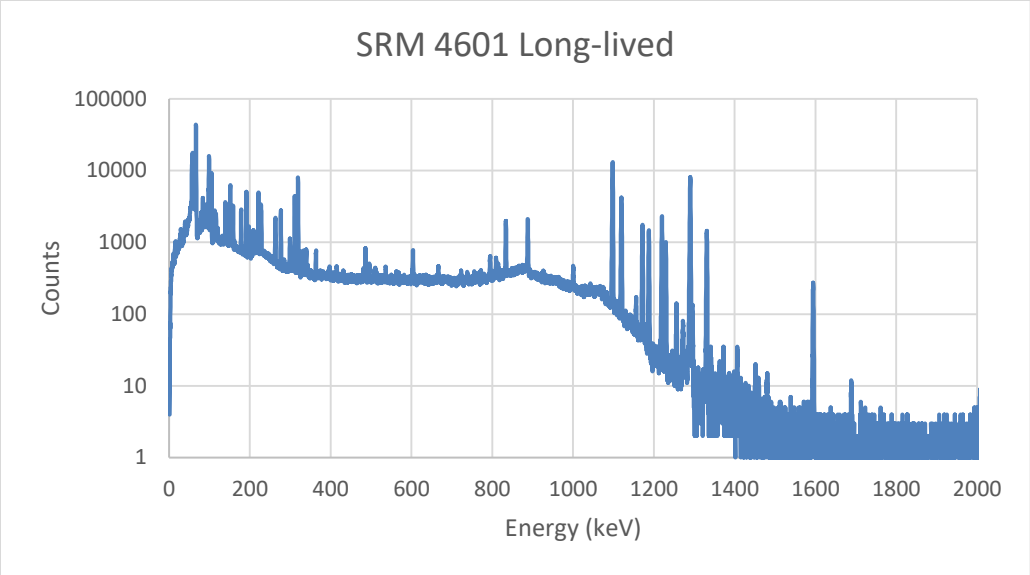

Figure 14: SRM 4601 Long-lived Spectrum

The area of each gamma-ray peak corresponds to an activity for the corresponding radioisotope. However, since the majority of nuclides identified emit multiple gamma-rays weight mean activities are displayed.

3.3.1 Calculation of Weight-mean Activity and Uncertainty

Weight-mean activity is defined as the inverse of the variance as shown as

$$w_i = \frac{1}{\sigma_i^2} \tag{3.1}$$

where σ_i^2 comes from Poisson statistics and is the variance of the activity of each photopeak of the given nuclide. In addition to counting statistics the uncertainty of the weight-mean activity is function of efficiency uncertainty, branching ratio uncertainty, and half-life uncertainty. The weighted mean is then calculated using the equation below:

$$\bar{x} = \frac{\sum_{i=1}^{n} \frac{x_i}{\sigma_i^2}}{\sum_{i=1}^{n} \frac{1}{\sigma_i^2}} \tag{3.2}$$

where x_i is the activity calculated from each gamma-ray emission of the nuclide. The uncertainty of the weighted mean is then calculated as

$$\sigma_{int} = \sqrt{\frac{1}{\sum_{i=1}^{n} \frac{1}{\sigma_i^2}}} \tag{3.3}$$

3.4 Creation of Nuclide Identification Libraries

For nuclide identification and quantification, Nuclide Identification (NID) Libraries were created that include the activation and fission product capabilities. For the NID library, probabilities of emission under 1% were generally ignored, but an exception had to be made for Pu-239 due to very low probability of emission for all of its gamma-rays. Parent-daughter information was included for relevant fission products, for example, Ba-140 decays to La-140 which decays to the stable Ce-140. This means the La-140 found in the sample could be a result of La-139 activation, the beta decay of Ba-140 after Ba-139 activation, or fission and it is important to know which path it took to reach La-140.

In order to create the NID libraries the peak locate and peak area functions were performed with GENIE 2000. Now that the energies of each peak are identified, the radioisotope corresponding to that energy needs to be determined. One by one, each peak energy was plugged into the AtomKaeri table of gamma rays to determine a potential isotope. For low energy gammas especially, there were many radioisotopes emitting photons within 1 keV of the peak centroid. In order to select the correct radioisotope a number of factors was taken into account. First and

foremost; the isotope had to be made through either neutron activation, or fission. So, any isotopes that are proton-rich, typically undergoing beta minus decay, are eliminated.

The next factors taken into account were branching ratio and whether or not the isotope had multiple gamma lines. If the isotope had multiple other gamma lines with a relatively high branching ratio, the next step was to see if the spectrum contained peaks at those energies as well. As mentioned, typically branching ratios less than 1% were ignored, but on occasion branching ratios slightly higher were ignored as well. For example, I-132 has a very large number of gamma lines with branching ratios of a few percent, so for I-132 branching ratios under 5% were ignored. Finally, half-life was used as the last criteria when selecting the most likely radioisotope. For the short-lived spectrum, the largest half-life was the 46.594 days of Hg-203 and the smallest was the 2.245 minutes for Al-28. For the medium-lived half-lives the shortest was for Xe-135 which is 9.14 hours, and longest was for Co-60 which is 1925.26 days. A few exceptions were made, first, with a count time of two hours, K-40 ($T_{1/2} = 1.248 * 10^9\ years$) was present and included in the NID library. Second, daughter nuclei with short half-lives were included because they are still being produced throughout the two-day decay time. For example, Nb-97 was present in the sample despite its 71.1-minute half-life because it's the decay product of Zr-97 which has a half-life of 16.749 hours. Finally, for the long-lived isotopes the main focus was on lower limits, of which the shortest half-life present in the sample was the 46.5-hour half-life of Sm-153. Again, exceptions were made for daughter isotopes.

After creating extensive NID libraries, there were still unidentified peaks. The energy of the peak would be looked at in AtomKaeri and in some cases no reasonable isotope would be present. Upon further review, the peaks of isotopes such as Co-60 and Na-24 were not perfectly calibrated.

For instance, the peaks of Na-24 were centered at 1368.1 keV and 2751.9keV instead of 1368.633 keV and 2754 keV respectively, in some cases, even the annihilation peak was a full keV away from 511keV. A second order polynomial energy vs channel number calibration was performed using a handful of peaks that were known, and is shown in Table 3. The calibration was a second order polynomial because the preamplifier has a nonlinear response. It is a very small, negative effect, that's why the high energy peak of Na-24 was off by so much compared to the lower energy peak. The recalibration led to the identification of more peaks, but there was still room for improvement.

Table 3: Energy Calibration Input

Isotope	Energy (keV)
W-187	72
Mo-99	181
La-140	328.8
Annihilation	511
W-187	685.8
Mn-54	834
Co-60	1171
Co-60	1333
Na-24	1368.633
K-40	1524
Na-24	2754

After using the interactive peak fit function in GENIE and getting a closer look at the unidentified peaks, it appeared that in some cases, what was thought to be one peak was really two peaks very close together. This was a problem for peaks at low energies. Using a similar approach as in the previous paragraph, the resolution was recalibrated. Again, known peaks were used, although the annihilation peak was omitted for this calibration. The calibration required the area and Full Width Half Max (FWHM) of the peaks. This was achieved by marking both sides of the peak with the cursor, which in it of itself is subjective and prone to uncertainty. However, this recalibration provided the ability to distinguish between peaks and ultimately identify more isotopes.

3.5 Calculation of Critical Limit and MDA

The activity was given in μCi, which can be simply converted into Bq/g by multiplying by 37000 (Bq/μCi) dividing by the mass of the sample (in grams). The critical limits found using the Currie MDA function on GENIE 2000. The critical limit, L_C, is described in Equation 3.4 (Currie).

$$L_C = k_{1-\alpha} * \sigma_0 \tag{3.4}$$

Where $k_{1-\alpha}$ typically 1.645 corresponding to the z-score associated with a 95% confidence, σ_0 is the background count error. In the case of the gamma spectroscopy of the SPUD samples the background is the counts from the Compton continuum and the error follows poison statistics. Equation 3.5 converts the critical limit in counts to a critical activity, A_C, of the source.

$$A_C = \frac{L_c}{\varepsilon B t} = w \tag{3.5}$$

ε is the detector efficiency, B is the branching ratio, and t is the acquisition time. The minimum detectable activity (MDA) is found using the same logic to convert detection limits into MDA. The critical level is the minimum number of counts where radioactivity can be confirmed.

If an equal chance of false negatives and false positives are confirmed ($k_{1-\alpha} = k_{1-\beta}$), the detection limit, L_D, is described using Equation 3.6 (Currie).

$$L_D = L_C + k_{1-\beta}\sigma_0 \tag{3.6}$$

Since the k values are the same, it is apparent that the detection limit is just twice the critical limit and can easily be converted to activity as shown in equation 3.5.

3.6 Results

Table 4 shows the weight-mean activities and uncertainties (1 σ is provided in the table) for nuclides identified in the 10-second irradiation in the tPNT facility. Gamma ray spectra were acquired for ten minutes following a ten-minute decay time. The NIST SRM 4600 had less nuclides identified since it had one third of the mass of the SRM 4601 sample for this analysis. Both activation products and fission products are quantified. If a nuclide was below the critical limit, it was noted in the table. The uncertainty was calculated from the GENIE software as noted in the previous section. Sources of error that were taken into account include branching ratio error, half-life error, efficiency error and count error. The uncertainty of sample mass, and all three time measurements (irradiation, acquisition, and decay) were ignored due to the incredible accuracy of time and mass measurements of modern day instruments.

Table 4: Nuclides from 10-s irradiation in tPNT facility followed by 10-minute decay

Nuclide	**NIST SRM 4600** **Wt. mean Activity** (Bq/g)	**NIST SRM 4601** **Wt. mean Activity** (Bq/g)
Na-24	1.36 (± 0.17)E03	1.18(± 0.17)E03
Mg-27	1.41(± 0.04)E04	6.07(± 0.21)E03
Al-28	1.17(± 0.03)E05	5.03(± 0.33)E03
Ca-49	1.78(± 0.07)E04	7.66(± 0.32)E03
V-52	1.64(± 0.1)E04	1.62(± 0.59)E03
Mn-56	2.03(± 0.01)E05	1.57(± 0.01)E05
Kr-85m	< 228	862(± 40)
Rb-89	< 827	2.84(± 0.25)E03
Sr-92	< 701	485(± 213)
Y-92	< 2.77E03	***
Nb-97	< 659	***
Zr-97	< 450	629(± 148)
Cs-138	< 1.22E03	3.12(± 0.17)E03
Xe-138	< 1.22E03	3.89(± 0.17)E03
Ba-141	< 666	3.77(± 0.13)E03
La-142	< 1.59E03	3.53(± 0.43)E03
Hg-203	< 384	607(± 188)
Pa-233	< 882	1.88(± 0.12)E03
U-239	1.14(± 0.03)E04	6.70(± 0.10)E03

*** all of the daughter nuclide activity is due to the parent activity

Table 5 shows the results for the gamma-ray acquired after the 30-minute irradiation in the 3-EL(Cd) facility. A combination of fast and epithermal flux was achieved in this facility as the cadmium liner absorbed the vast majority of thermal neutrons, rendering the thermal flux negligible. Samples decayed for two days prior to a 2-hour gamma-ray acquisition. Activation products and fission products were quantified. It's important to note that Ba-140 is expected to be present in SRM 4600 due to the presence of La-140 and other fission products. However, the primary peak of Ba-140 is at 537 keV with a branching ratio of 24% compared to the primary peak of La-140 which has a branching ratio of 95% at 1596 keV. The smaller branching ratio combined with the significantly larger Compton continuum at 537 keV resulted in La-140 getting detected and Ba-140 being below the critical limit.

Table 5: Nuclides from 30-min irradiation in 3-EL(Cd) followed by 2 days decay

Nuclide	**NIST SRM 4600** **Wt. mean Activity** (Bq/g)	**NIST SRM 4601** **Wt. mean Activity** (Bq/g)
Na-24	9.398 (± 0.98)E03	9.337 (± .082)E04
K-40	1.321 (±.046)E03	2.586 (± .036)E04
K-42	2.050 (± .173)E03	2.215 (± .145)E04
Cr-51	874 ± 108	9.337 (± 1.016)E03
Mn-54	632 ± 60	7.827 (± .485)E03
Fe-59	861 ± 49	7.872 (± .419)E03
Co-60	94.0 ± 15.5	874 ± 182
Ga-72	654 ± 52	5.538 (± .412)E03
As-76	2.957 (± .105)E03	5.904 (± .275)E04
Nb-97	78.9 ± 37.3	***

Zr-97	47.6 ± 13.0	9.154 (± .266)E03
Mo-99	1.840 (± .121)E03	2.682 (± .114)E04
Tc-99m	***	***
Ru-103	< 150	1.56E-04 ± 2.42E-05
Sb-122	371 ± 22	6.62E-04 ± 4.06E-05
I-131	< 160	7.21E-04 ± 7.34E-05
I-132	***	***
Te-132	485 ± 51	1.250 (± .046)E04
I-133	40.5 ± 21.6	1.318 (± .029)E04
Xe-135	5.2 ± 17.0	1.025 (± .021)E04
Ba-140	< 536	5.035 (± .431)E03
La-140	632 ± 23	***
Ce-141	< 311	1.451 (± .170)E03
Ce-144	1.019 (± .162)E03	9.337 (± 1.369)E03
Sm-153	3.030 (± .016)E04	2.961(± .014)E05
Ho-166	< 2.554E03	1.250 (± .133)E04
Tm-170	1.926 (± .543)E03	9.657 (± 2.220)E03
Ta-182	3.109 (± .037)E03	3.492 (± .045)E04
W-187	6.401 (± 1.11)E03	5.858(± .068)E04
Pa-233	497 ± 33	5.035 (± .297)E03
Np-239	3.720 (± .017)E04	3.666 (± .015)E05

*** all of the daughter nuclide activity is due to the parent activity

Table 6 shows the results from the 1-hour irradiation in the RSR facility. These samples decayed for two weeks followed by an 8-hour gamma ray spectrum acquisition. A large suite of fission products was quantified with multiple parent-daughter decay chains. For these decay chains the daughter activity is largely due to the ingrowth from the parent as expected. The higher fission product activities in the SRM 4601 sample are due to the 22% U-235 enrichment of the sample.

Table 6: Nuclides from 1-hour irradiation in RSR followed by 2 weeks decay

Nuclide	**NIST SRM 4600** **Wt. mean Activity** (Bq/g)	**NIST SRM 4601** **Wt. mean Activity** (Bq/g)
Sc-46	544(± 9)	844(± 12)
Cr-51	1.01(± 0.01)E04	1.07(± 0.01)E04
Mn-54	585(± 9)	759(± 14)
Fe-59	1.15(± 0.01)E03	1.43(± 0.03)E04
Co-60	884(± 6)	1.13(± 0.01)E04
Zn-69m	< 12.7	128(± 5)
Ga-72	740(± 12)	< 25.3
Rb-86	258(± 71)	125(± 52)
Sr-90	< 12.0	31.6(± 3.3)
Nb-95	***	***
Zr-95	28.7(± 7.3)	2.32(± 0.02)E03
Mo-99	925(± 38)	1.65(± 0.04)E03
Tc-99m	297(± 4)	2.44(± 0.01)E03
Ru-103	39.2(± 2.1)	1.52(± 0.01)E03
Sb-122	33.7(± 3.3)	51.8(± 4.9)

Nuclide	**NIST SRM 4600** **Wt. mean Activity** (Bq/g)	**NIST SRM 4601** **Wt. mean Activity** (Bq/g)
I-131	68.5(± 2.3)	2.73(± 0.04)E03
I-132	***	***
Te-132	90.7(± 3.7)	1.70(± 0.01)E03
Xe-133	266(± 4)	4.67(± 0.02)E03
Cs-134	120(± 4)	156(± 4)
Ba-140	137(± 9)	5.77(± 0.06)E03
La-140	***	***
Ce-141	190(± 4)	3.53(± 0.03)E03
Ce-144	28.5(± 12.9)	< 395(± 24)
Nd-147	248(± 5)	2.09(± 0.04)E03
Eu-152	20.1(± 1.4)	25.8(± 2.6)
Sm-153	1.54(± 0.01)E03	55.1(± 7.9)
Tm-170	7.59(± 0.07)E03	< 712
Hf-181	24.1(± 2.2)	37.7(± 3.9)
Ta-182	5.51(± 0.01)E03	5.98(± 0.02)E03
Pa-233	1.24(± 0.01)E03	1.47(± 0.02)E03
Np-239	1.68(± 0.01)E03	888(± 18)
Pu-239	4.44(± 0.03)E06	2.85(± 0.06)E06
Am-241	3.41(± 0.02)E06	4.09(± 0.02)E06

*** all of the daughter nuclide activity is due to the parent activity

This work quantifies the activation products and fission products produced through neutron activation of the NIST SPUD samples. Three irradiations of each SPUD sample were conducted followed by gamma ray spectroscopy. Different nuclides are quantifiable depending on the irradiation, decay, and counting methodology. Similar activations could be utilized to produce quality control and quality assurance measurements in nuclear laboratories that may analyze post-detonation samples. In general, the results for the SRM 4600 and 4601 compared within statistical expectations. However, there were multiple cases where radionuclide activities were clearly divergent between the two samples. These differences may be due to sample inhomogeneities that are likely when small sample sizes are utilized (e.g., the sample size for the 3-EL irradiations was less than 0.06g). Larger samples could be utilized, but neutron fluences for the irradiation would have to be reduced by more than an order of magnitude so that sample activities would not induce significant detector deadtime.

Further work should be conducted to determine the optimum point between sample size and irradiation methodology. As part of this optimization study, one should consider the nuclides of interest for post-detonation debris analysis. Time between the event and the start of the gamma-ray spectrum acquisition need to be considered to assess a suitable sample composition.

CHAPTER 4: SELF-ATTENUATION ANALYSIS

4.1 Motivation

It is important to have as precise data as possible when evaluating the gamma spectra. Specific information about the radioisotopes present in the debris can help identify what the IND is composed of and subsequently, where it came from. The radioactive debris will come in all shapes, sizes, and densities so it will be of vital importance to be able to accurately measure radioactivity regardless of those variables. An analysis of the attenuation of gamma rays as a function of source density and gamma ray energy was performed using an MCNP input file.

4.2 Method

The input file was designed to generate the peak efficiency of an HPGe detector as a function of source energy and density. To keep all other factors consistent, the input file was created to model a source of a constant size and a constant distance away from the HPGe detector. The code was run many times only changing the source material (atomic number and density) to include a distribution of densities from 1.065 g/cc (hydrochloric acid) to 19.86g/cc (plutonium) and is shown Table 7.

Table 7: Material Density

Material	Density (g/cc)
HCl	1.065
Carbon	1.6
Aluminum	2.7
Titanium	4.51
Vanadium	6.1
Iron	7.37
Copper	8.96
Silver	10.49
Lead	11.34
Tantalum	16.65
Gold	19.32
Plutonium	19.86

The source modeled via the MCNP input file was time-independent and uniformly distributed. The assigned gamma-ray energies and relative frequencies are shown in Table 8.

Table 8: Original MCNP Source Definition

Isotope	Energy (keV)	Relative Frequency
Am-241	59.5	0.0292
Cd-109	88	0.4038
Co-57	122.1	0.0092
Ce-139	165.9	0.0138
Hg-203	179.2	0.0297
Sn-113	391.7	0.0236
Sr-85	514	0.1212
Cs-137	661.6	0.0116
Y-88	898	0.0369
Co-60	1173.2	0.0182
Co-60	1332.5	0.0182
Na-24	1368.6	0.1212
Y-88	1836.1	0.0369
Na-24	2754	0.1212

The energies and relative frequencies were selected based off the multi-gamma standard shown in the previous chapter (Table 2) with a few minor changes in attempt to optimize the energy distribution of the photopeaks. Pb-210 was removed as it was only 13 keV less than the Am-247 peak; Na-24 was added to increase the highest energy to 2754 keV; and Sr-85 was added to provide an energy in between the 661.7 keV Cs-137 peak and the 391.7 keV Sn-113 peak. The relative frequency of each peak is proportional to the activity in the multi-gamma standard of the corresponding peak, with three exceptions. The exceptions are for the photopeaks that weren't in the multi-gamma standard (i.e. Na-24 and Sr-85) for which the relative frequency corresponding to the activity of the Pb-210 that was removed was split equally between the three peaks, hence their equal values.

4.3 Calculation Process

Peak efficiency, ε, from the MCNP code is calculated in Microsoft Excel using the equation below where NPS is the total number of photons run in the MCNP code, A is peak area in counts and F is relative frequency given to each photopeak.

$$\varepsilon = \frac{A}{F*NPS} \tag{4.1}$$

The data from MCNP was then plugged into MATLAB and the surface fit tool was used to generate a best-fit equation that solves for peak efficiency as a function of material density and gamma ray energy. The actual data used in the surface fit was the natural log of the peak efficiency, the density, and the natural log of the energy. This is because the efficiency vs energy curve changes very drastically at low energies and taking the natural log of energy and efficiency allows for a more accurate surface fit; an example is provided on the following page.

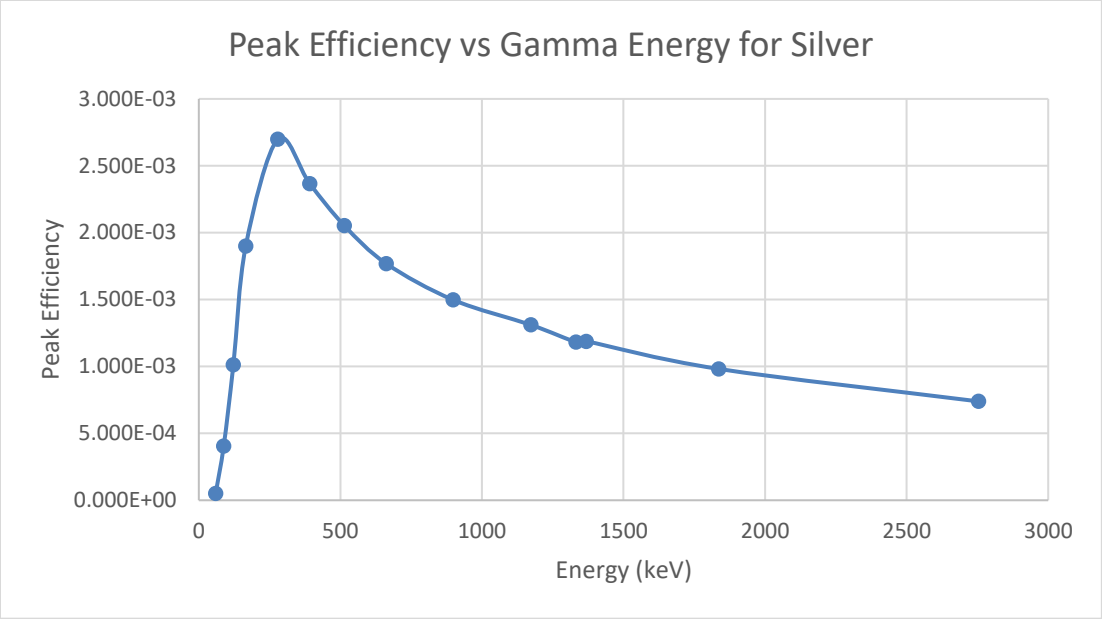

Figure 15: Silver Peak Efficiency vs Energy

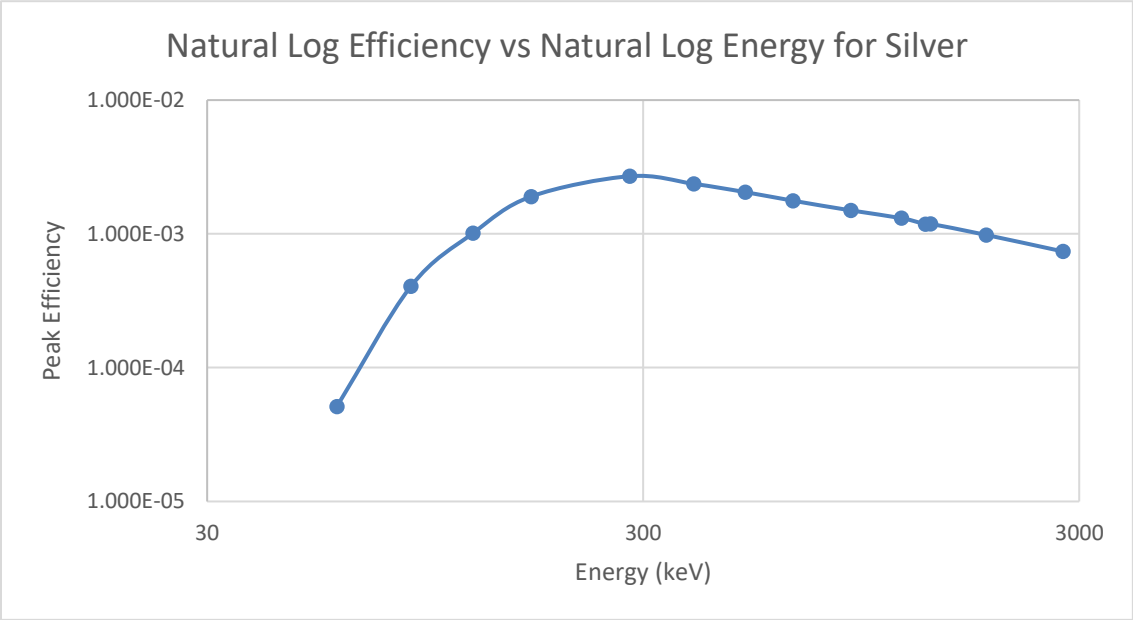

Figure 16: Silver Natural Log of Peak Efficiency vs Natural Log of Energy

The surface fit was polynomial; third order for density and fourth order for natural log of energy. The equation generated from the first set of data is given below where x is density, y is

natural log of energy, and the remaining integers are the coefficients generated in MATLAB. Since MATLAB was used to create the surface fit equation there were only a few possibilities of surface-fit types. There are three types of fits MATLAB allows; LOWESS, interpolant, and polynomial, of which, polynomial is the only surface fit that provides an equation. The other two are non-parametric fits. Within the polynomial fit MATLAB allows the user to select a polynomial of any order from one to five for each variable. A fifth order polynomial was selected for both variables and MATLAB issued a warning stating "the equation is badly conditioned," so the order of each variable was reduced until the r-squared showed a significant change. This resulted in a third order polynomial in density and a fourth order polynomial in natural log of energy.

$$\ln(\varepsilon) = f(x,y) = -183.3 + .9692x + 112.7y - .05051xy - .7848x^2 - 25.97y^2 + .005439xy^2 - .01492yx^2 + .2036x^3 + 2.587y^3 - .0007622xy^3 + .003083yx^3 - .01585(xy)^2 - .09427y\text{^}4 \quad (4.2)$$

Although the coefficients of the surface fit are provided to four significant figures here, sixteen significant figures were used when solving for efficiency from the equation. When only four significant figures were used, the data was very inaccurate because density and natural log of energy are raised to the third and fourth power respectively, and slight errors in this coefficient propagate into massive errors. To put this in perspective, the maximum density (21) raised to the third power is 9261, but the natural log of peak efficiency ranges from about -6 to -10. So, an error of only 10^{-5} in the x^3 coefficient at 21g/cc, would change the natural log of efficiency by about .1, say from -7.6 to -7.5. Although this may not seem like a large error, once the exponent is taken, the error becomes 10.5%. Sixteen was the number of significant figures selected because it is what MATLAB provides when using the "format long e" command, and it generates accurate values. The surface fit has an r-squared value of .9563 and is provided in Figure 17.

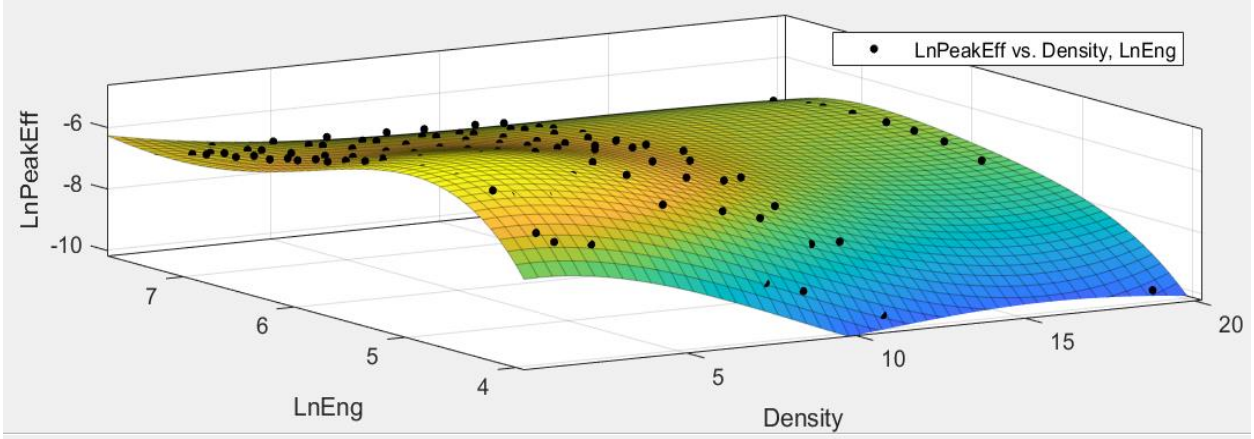

Figure 17: Original Material Surface Fit

The whole idea behind this analysis is to use the surface fit equation on a sample that has at least one multi-gamma isotope (i.e. Sodium-24 is known to emit a 1368.6 keV gamma-ray with a branching ratio of 99.9936% and a 2754 keV gamma-ray with a branching ratio of 99.855%). It is vital that a multi-gamma isotope is present in the sample otherwise there would be two unknowns for every equation; the activity and the efficiency. When computing the ratio of peak efficiencies of two photopeaks originating from the same isotope, the activity can be divided out producing an equation with one unknown. The equations below are used to help illustrate this idea.

$$\varepsilon = \frac{A}{\alpha * B} \tag{4.3}$$

$$EffRatio = \frac{\varepsilon_1}{\varepsilon_2} = \frac{\frac{A_1}{\alpha * B_1}}{\frac{A_2}{\alpha * B_2}} = \frac{A_1 B_2}{A_2 B_1} \tag{4.4}$$

In the equations above A and ε are still peak area and efficiency respectively, but since its actual radiation in a detector, B is the branching ratio, and α is the activity which is analogous to relative frequency and NPS respectively from Equation 4.1 used to calculate peak efficiency from the MCNP code.

In a SPUD sample that contains a multi-gamma isotope the ratio of peak efficiencies will be calculated using Equation 4.5. That ratio value, along with the energies of the gamma-rays at

which the ratio was calculated (again, 1368 keV and 2754 keV if Na-24 is present) will go into the MATLAB code that was created to in turn provide an effective density of the sample. Once the effective density is known, it can be plugged into the surface-fit equation (as the x variable in Equation 4.2) to provide the peak efficiency as a function of energy only. Equation 4.5 is used to illustrate this.

$$\frac{\varepsilon_1}{\varepsilon_2} = \frac{e^{\ln(\varepsilon_1)}}{e^{\ln(\varepsilon_2)}} = \frac{e^{f(x,y_1)}}{e^{f(x,y_2)}} = e^{f(x,y_1)-f(x,y_2)} \tag{4.5}$$

In Equation 4.5 *f(x,y)* is the surface fit equation, $\frac{E_1}{E_2}$ is the ratio of efficiencies, and the energy of the photopeaks of interest are y_1 and y_2, which are known quantities, therefore x (the density) is the only unknown, and can be solved for.

4.4 Methodology

The success of this process is almost entirely dependent on the accuracy of the surface fit equation, which is dependent on the data from the MCNP input file. Despite the high r-squared value, the first set of data isn't as accurate as needed.

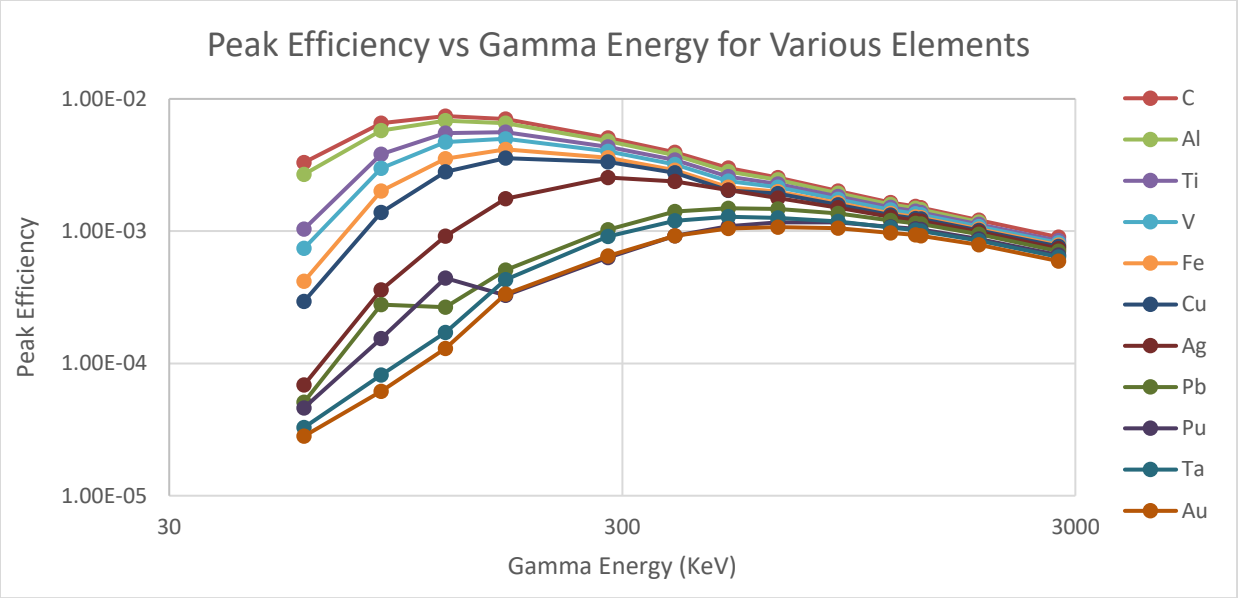

Figure 18: Peak Efficiency vs Energy for Many Materials

Figure 18 shows the peak efficiency vs energy for each material. For the most part, the data isn't bad, but there are some problems. There are the jumps in peak efficiency for lead and plutonium at low energies. There is also overlap and crossing of the gold and plutonium.

One of the problems with these data is that the elements with higher density and higher atomic number tend to have K-edge effects, causing sharp turns in the peak efficiencies at the low energies that correspond with the K-edge. As shown in the figure below, the probability of gamma interaction increases as energy decreases, but for lead there is a sharp decrease of interaction probability as the energy approaches around 100 keV from the right. Essentially the k-shell electrons become transparent to the photons once it crosses that energy threshold.

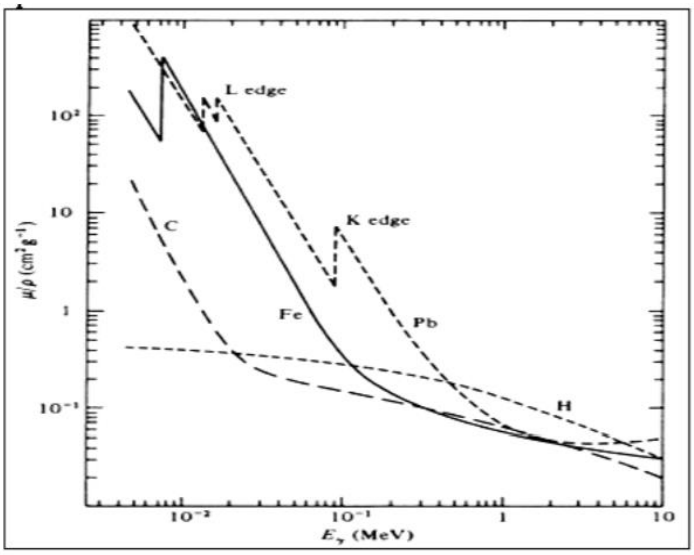

Figure 19 Edge Effects (Abdullah)

This decrease also helps to highlight another phenomenon that leads to the complexity of this fit, which is the changing atomic number of the samples. The probability of a photon-electron interaction changes with z. Although there isn't a way to determine the exact probability of a photoelectric effect interaction, it is proportional to the atomic number raised to the n power as described by the equation below (Knoll). Where n is between four and five, and W is the photon energy.

$$\tau \cong constant * \frac{Z^n}{W^{3.5}} \tag{4.5}$$

Another set of materials were selected in attempt to find materials in which the k-edge wasn't much of a factor. This proved difficult when attempting to find materials with densities over about 12 g/cc. The energy of the gamma lines was also expanded in attempt to produce a better fit; the energy and relative frequencies are displayed in the following table.

Table 9: MCNP SPUD Source Definition

Energy (keV)	Relative Frequency
67.75	0.08099
72	0.02557
100.11	0.02680
134.25	0.01955
152.43	0.01325
222.11	0.01428
229.32	0.00687
264.07	0.00681
479.53	0.05018
551.55	0.01159
618.37	0.01428
685.81	0.06265
772.87	0.00947
846.76	0.18653
1121.29	0.06650
1189.04	0.03112
1221.4	0.05138
1231	0.02191
1368.63	0.09434
1524.6	0.03412
1810.73	0.05074
2113.09	0.02685
2754	0.09422

These energies were selected because they correspond to photopeaks of radioisotopes found in the SPUD samples. Specifically, W-187, Ta-182, Mn-56, Na-24 and K-40. All of these elements have multiple photopeaks except K-40, however K-40 was used because it is a naturally occurring radioisotope, and it provides a favorable energy point (1524.6 keV). The efficiency vs energy curves are provided in the following figure.

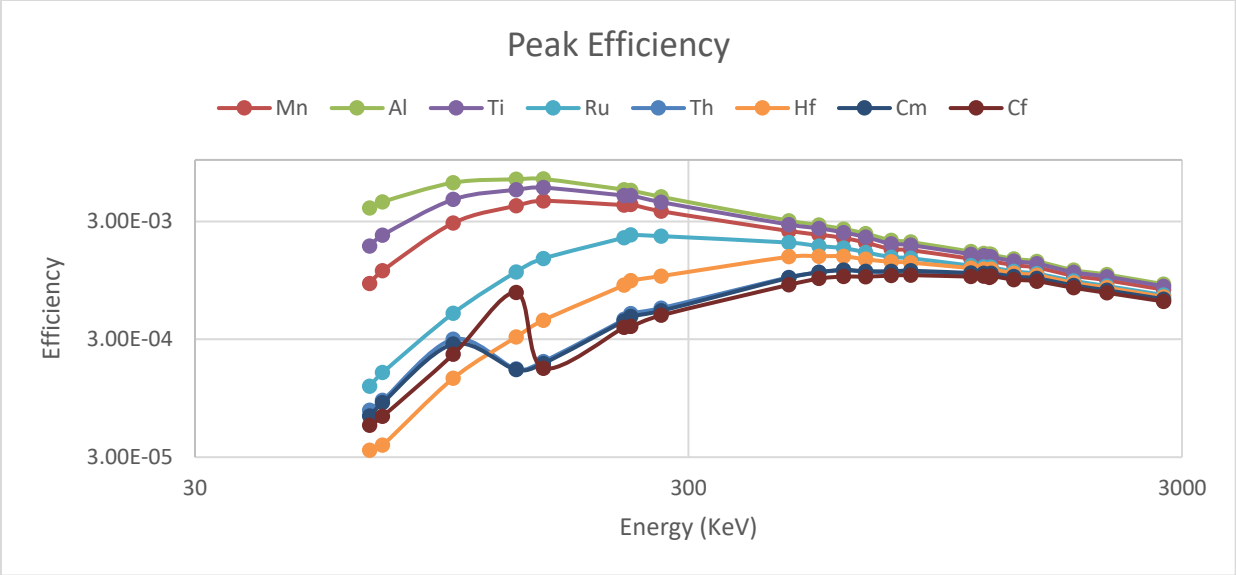

Figure 20: Peak Efficiency vs Energy for Various Materials Using SPUD Sources

Regardless of the number of materials used in the trial, there were always some edge effects present. Adding the extra data points did not make the surface fit much better (r-squared is .9611) as shown below.

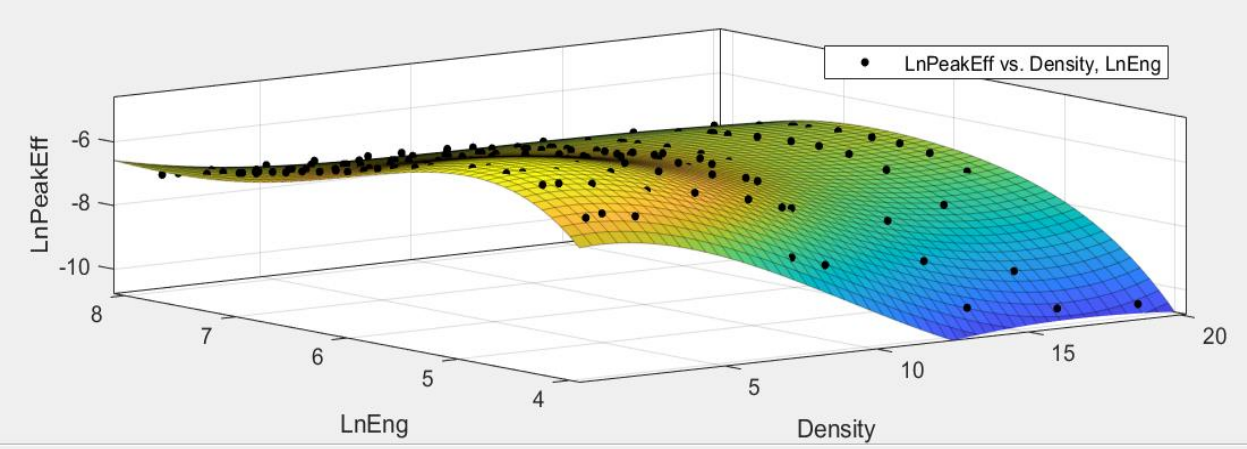

Figure 21: Surface fit of Materials Using SPUD Sources

Although atomic number and density are positively correlated, it isn't an exact correlation. In order to reduce variables, the MCNP code was changed so that carbon (z=6) would remain as the constant material, but the density would change from 1g/cc to 21g/cc to get roughly the same

density range as the first two trials. The efficiency curves for each density are shown in Figure 22; note only the odd densities are shown to make it easier to see.

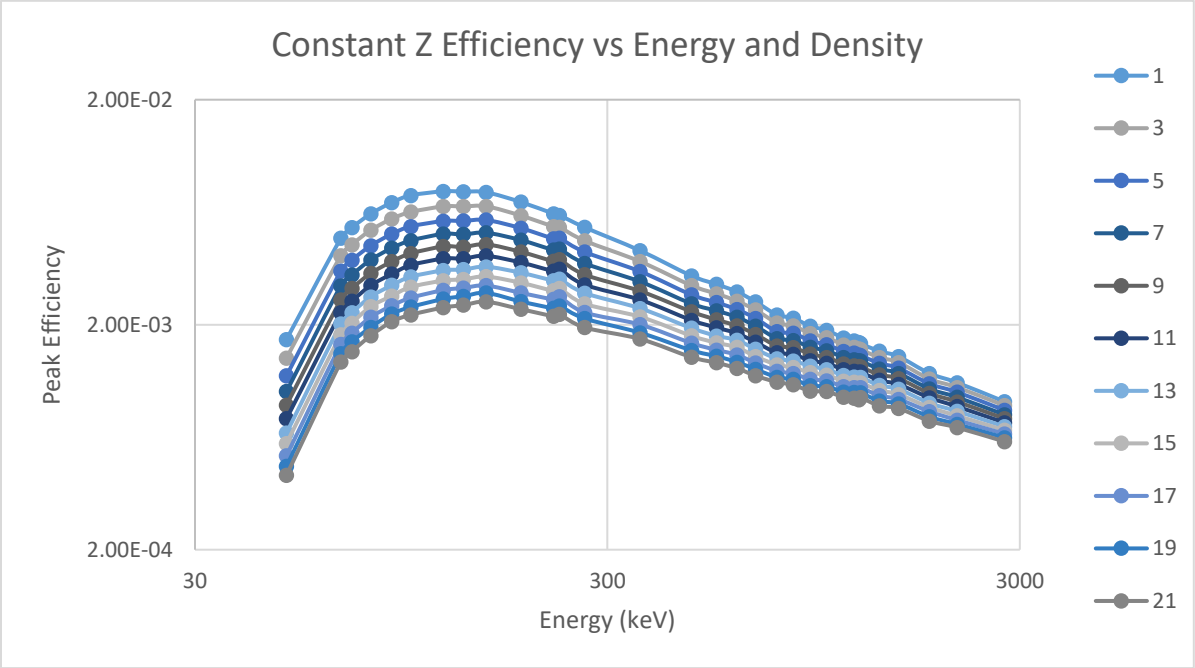

Figure 22: Peak Efficiency vs Energy for Variable Density Carbon

This graph appears better than the two previous, but what about the surface fit?

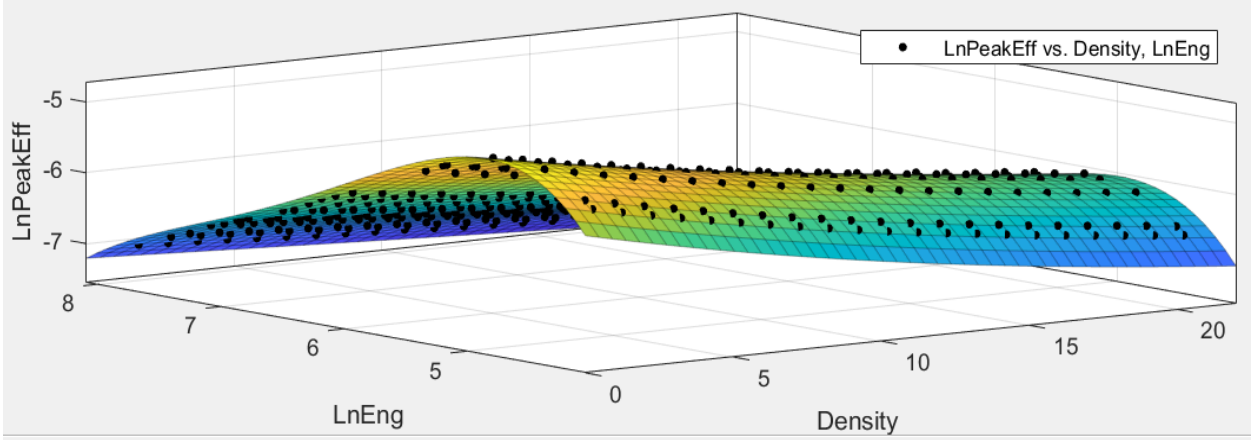

Figure 23: First Carbon Surface Fit

There was a stronger correlation in the surface fit equation as r-squared went from .9611 to .9868 using carbon. However, even this small error magnified when converting back to peak efficiency (from natural log) there error wasn't negligible. It was also noticed that at high densities the peak areas were small (peak area was 870 counts for the 67.75keV peak at 21g/cc), creating relatively large variances in the peak efficiencies due to count error. This was combatted by performing a sensitivity test. The particle histories run in the MCNP code were increased for a second and third test to see how accurate the surface fit could be. To supplement the increased number of particle histories, the following additional gamma ray lines were added to the MCNP input file in attempt to get a more accurate peak: 50, 80, 90, 185, 360, 930 and 1020 keV. The table below shows the lowest peak area, and the r-squared of the fit corresponding to each trial.

Table 10: Sensitivity Test Data

Carbon Trial #	Lowest Peak Area	R-squared
1	870	.9868
2	8,348	.9967
3	54,907	.9966

As apparent in Table 10, the low counts made the surface fit slightly worse for the first trial, however, the increased peak areas didn't matter between the second and third trial. It's not surprising as count error is $A^{-1/2}$, which corresponds to just a 1.09% error in the second trial, and a 0.43% error in the third trial. Also note that this is the lowest peak area; most of the peak areas are much higher than these. There is also uncertainty that MCNP provides in the F8 tally which was between about 0.1% to about 1%.

The next step was to determine how accurately the surface fit equation would model another set of data. Another set of data was created using MCNP. The densities chosen were all half-integers from 1.5g/cc to 21.5g/cc and the energies are specified in Table 11, and the data is referred to as the comparison data as it was compared to the surface fit equation to evaluate its accuracy.

Table 11: Source Information for Comparison Data

Energy (KeV)
59
110
205
310
420
505
585
980
1300
1450
1660

When those energies and densities were plugged into the surface fit equation it always calculated a peak efficiency within 2% of the comparison data. The one exception to this was that the peak efficiency of the 59 keV peak was on average 9.571% higher in the surface fit equation than in the comparison data. This is because the surface-fit isn't very accurate at low energies, which is due to the extremely high slope of the peak efficiency vs energy graph at low energies, and although it wasn't corrected in this thesis, it could be improved by using more low energy gamma ray lines in the MCNP model. The average percent error and standard deviation are shown for the surface fit vs the comparison data in the following table. The full data is provided in the appendix, but the standard deviation is shown in Table 12 to illustrate that in addition to the low average error, the spread of such error is also small.

Table 12 Average Error of Surface Fit

Energy (keV)	Average Error (%)	Standard Deviation of % Error
59	9.571	0.954
110	-0.667	0.438
205	0.068	0.460
310	0.745	0.288
420	0.035	0.139
505	0.165	0.240
585	-0.605	0.133
980	-0.125	0.185
1300	0.976	0.314
1450	1.060	0.263
1660	0.517	0.069

Since the fit wasn't incredibly accurate for the 59 keV peak, the 50 keV peak data was removed from the surface fit to increase the accuracy of the rest of the energy peaks. This worked, as the R-squared increased to .9997, and .9998 for carbon trials 2 and 3 respectively. The tradeoff of this improved accuracy is that the equation fit cannot be used to model efficiency of an HPGe of gamma rays below 67.75 keV. The final surface fit is shown below.

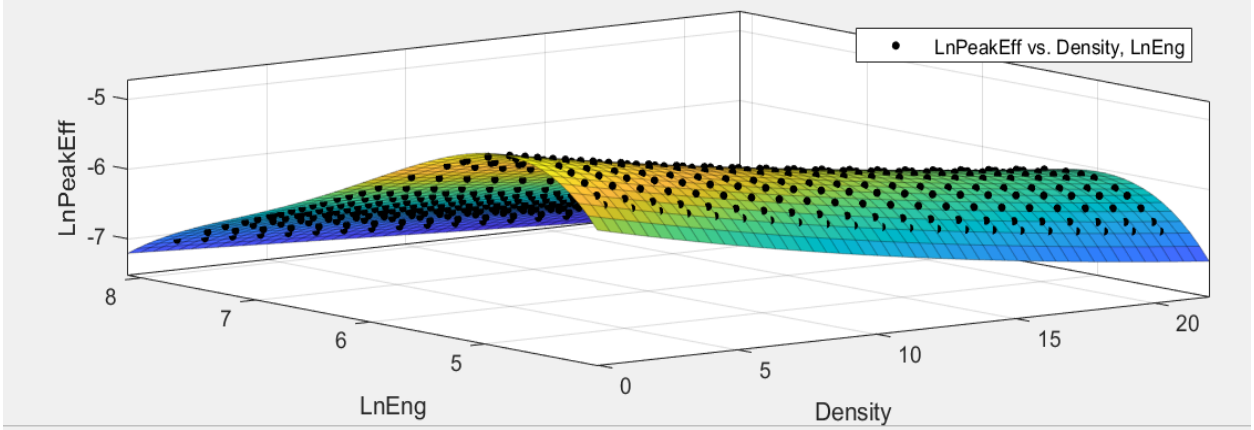

Figure 24: Carbon Trial 3 Surface Fit (No 50 keV Line)

The next way to verify the surface fit equation was to use the ratio of the efficiency of two peaks to determine density. The original MATLAB file was updated with the new surface fit, the comparison data was plugged in to see how accurate the output density would be. The following table shows the percent error in the density calculated from the ratio of efficiencies at the given energies.

Table 13: Accuracy of Density-calculating Algorithm

Ratio	1.5	2.5	3.5	4.5	5.5	6.5	7.5	8.5	9.5	10.5	11.5	12.5	13.5	14.5	15.5	16.5	17.5	18.5	19.5	20.5	21.5
110/980	1.114	-0.677	-1.253	-1.342	-0.714	-0.347	-0.903	-0.974	-1.170	-1.103	-0.871	-0.727	-0.534	-0.673	-1.216	-1.360	-1.814	-2.221	-2.797	-2.957	-3.010
205/1300	-8.960	-5.688	-5.023	-5.002	-4.305	-3.263	-3.543	-3.725	-3.007	-2.728	-2.043	-1.834	-1.745	-1.735	1.073	0.573	0.637	0.669	0.654	0.179	-0.017
310/1450	-2.900	-2.028	-0.991	-2.160	-1.222	-1.432	-0.795	-0.811	-0.746	0.239	1.190	1.572	1.438	0.543	3.335	3.338	3.329	3.711	3.551	2.987	2.535

The negative numbers are in red. The algorithm calculates the density to within a few percent error in almost every case. The exception is for low densities for the 205 keV to 1300 keV efficiency ratio which gets to -8.96% error at 1.5 g/cc. Overall this surface fit method has proven to be accurate.

CHAPTER 5: CONCLUSIONS

There are two focal points of this work; to correctly characterize the composition of the SPUD samples, and to create a method for accurately determining detector efficiency as a function of source energy and density. The first point involved creation of extensive NID libraries, and the effective use and occasional recalibration of GENIE 2000 software. To accomplish the second point, an MCNP input file was created to model the source-detector system and many trials were run to acquire sufficient data. Then a MATLAB surface fit was created from the data, and a MATLAB code was written to produce the efficiency curve from the ratio of the efficiency at two known energies. Finally, comparison data was acquired, also via MCNP, to verify the results of the MATLAB code.

To evaluate the results of this thesis it's important to return to the statement of goals. First, the SPUD sample spectroscopy was achieved with reasonable accuracy. The SRM 4600 and the SRM 4601 were found to have the same isotopes, with an increased concentration of fission products in the SRM 4601. There were a few radioisotopes that were expected to be present in small quantities that weren't detected, but that's not uncommon when the expected activity is so close to the MDA. Again, there were some discrepancies between the SRMs which is likely do to the size and inhomogeneity of the samples. Second, the data from MCNP was able to create accurate surface fit equations with an r-squared value as high as .9998. Although the fit was less accurate at energies below the 67.75 keV peak and a density of 1.5g/cc; it was very accurate (within 3% error) between 110 keV and 2754 keV and between 2.5g/cc and 21.5 g/cc. For the 59 keV peak the error was consistently around 9.5%. Third, a MATLAB code was created to take the efficiency ratio at two energies and produce an effective density. Similar to the surface fit, this code was accurate within 3.5% with a few exceptions where the error reached a magnitude of about 9%.

There were a number of limitations in the SPUD analysis. The dead-time effects on the short-lived samples was 2.63% for SRM 4600 and 4.77% for SRM 4601. Although the neutron flux in an IND can't be replicated, a neutron energy spectrum could be better approximated than in this experiment. The samples did get fast and epithermal neutrons when placed in the 3-EL, but mostly thermal neutron fluxes were present in the RSR and the PNT, which result in more fissions and less activations than the fast neutron flux associated with an IND. There would also be a much higher neutron flux in the fissile material relative to the surrounding material during a real detonation. These two differences have opposite effects, so while it can't be said they cancel each other out, at least one helps combat the other. As shown in Table 1, the samples varied in size, which can alter the neutron activation and fission occurring during irradiation, as well as the self-attenuation of the gamma rays during acquisition. This work also did not attempt to model the heterogeneity of the samples, and how that effects the measurements.

No experiment is immune to limitations and the self-attenuation analysis had several. In the MCNP model, sum peaks were not taken into account. Given that the source was about 12cm from the detector, these effects would be small but it's not likely they'd be negligible. Dead-time effects were not modeled in MCNP either. MCNP tracks each particle individually, and therefore two photons would not be tallied at the same time. MCNP also doesn't deal with detector electronics, and therefore doesn't account for pulse pile-up. Both of these issues are exacerbated when comparing MCNP results to high-activity samples due to their high dead-time and probability of coincidence.

Another substantial limitation of MCNP HPGe modeling is the lack of accurate detector specifications, and the inability to physically model the detector. Part of this is due to the manufacturer's lack of detector specifications. There is also a dearth of knowledge of germanium behavior at the atomic level. There are impurities in the HPGe that can't be modeled in MCNP. The location and type of impurities are unknown. Ultimately, the best way to model the efficiency of an HPGe would be to create sources of a known radioactivity in the desired geometry, with the

desired material. The problem with that is that there are two unknowns in a post-detonation sample; the composition of the sample, and the activity, and you can't solve for one without the other. It's possible, given a calibrated detector for a source of the same size as the post-detonation sample, by measuring the density of the sample with a scale one could estimate the corrections needed to the calibration curve. This leads to the next problem with the self-shielding analysis; it's only valid for a material with six protons. In order to truly model the self-attenuation another series of MCNP files must be run to determine the detector efficiency as a function of z as well as energy and density. This would, of course, take a very long time, and corrections would need to be made for characteristic X-ray detection.

While the method chosen for this thesis was to keep the atomic number constant and just solve for efficiency as a function of energy and density there are other ways to model self-shielding. If atomic number changed as well, the complexity increases, but there are ways to characterize it. First, the k-edge could be treated wither of the following ways: ignore the data prior to the k-edge effect (low energy) of the high atomic numbers, or to apply a correction factor for the k-edge of materials above a certain atomic number. The use of atomic number as its own variable would be difficult as peak efficiency is now a function of three variables instead of two. Finally, one could also do two separate equations for above and below the efficiency climax of about 130keV. This could produce more accurate results, however, one would need use caution both when defining the energy at which to make the cutoff, and when modeling the efficiency near that threshold energy.

The methods shown in this thesis proved to be useful despite its flaws. With access to a computing cluster the MCNP approach to characterization of detector efficiency could be an effective technique without the cost of developing a plethora or sources, or the need to be exposed to actual radiation.

APPENDIX A. NUCLIDE IDENTIFICATION LIBRARIES

A.1 Short-Lived Library

Nuclide	Energy (keV)	Branching Ratio (%)
Na-24	1368.63	99.99
	2754.01	99.86
Mg-27	843.76	71.80
	1014.52	28.20
Al-28	1778.99	100.00
Ca-49	3084.40	90.72
V-52	1434.06	100.00
Mn-56	846.76	98.85
	1810.73	26.89
	2113.09	14.23
Br-84	802.20	5.99
	881.60	41.60
	1015.90	6.16
	1897.60	14.56
	2484.10	6.66

	3927.50	6.78
Kr-85m	151.20	95.40
	304.87	66.20
Rb-89	657.77	10.82
	947.73	10.00
	1031.92	62.90
	1248.14	45.92
	2195.92	14.47
	2570.21	10.69
Sr-92	1383.93	90.00
Y-92	934.47	13.90
	1405.40	4.78
Zr-97	743.36	93.09
Rh-103	306.10	5.01
	318.90	19.10
Sb-122	564.24	72.42
I-134	405.45	7.37
	595.36	11.10

	621.79	10.62
	677.34	7.94
	847.03	95.70
	857.29	6.70
	1072.55	14.93
	1136.16	9.09
	1806.84	5.55
Cs-138	408.98	4.66
	462.80	30.52
	547.00	10.76
	871.80	5.11
	1009.78	29.83
	1435.86	76.30
	2218.00	15.18
Xe-138	153.86	5.95
	258.41	31.50
	396.51	6.30
	434.56	20.32

	1768.26	16.73
	2004.75	5.36
	2015.82	12.25
Ba-141	190.33	45.50
	276.95	23.16
	304.19	25.16
	343.67	14.29
Ba-142	77.49	9.52
	255.30	20.60
	895.20	13.93
	949.10	10.65
	1078.70	11.52
	1204.30	14.30
La-142	641.28	47.40
	894.90	8.34
	1901.30	7.16
	2397.80	13.27
	2542.70	10.00

Hg-203	279.20	81.56
Pa-233	311.90	38.50
U-239	74.66	53.20

A.2 Medium-Lived Library

Nuclide	Energy (keV)	Branching Ratio (%)
Na-24	1368.63	99.99
	2754.01	99.86
K-40	560.18	99.99
K-42	1524.60	18.08
Cr-51	320.08	9.91
Mn-54	834.85	99.98
Fe-59	1099.24	56.50
	1291.59	43.20
Co-60	1173.23	99.85
	1332.49	99.98
Ga-72	629.97	26.13
	834.19	95.45

	894.33	10.14
	2201.59	26.87
	2507.72	13.33
As-76	559.10	45.00
	657.05	6.16
Nb-97	657.95	98.23
Zr-97	743.36	93.09
Mo-99	181.07	6.03
	739.50	12.26
	777.92	4.30
Tc-99m	140.51	89.00
Ru-103	497.08	91.00
	610.33	5.76
Sb-122	564.24	72.42
I-131	284.30	6.12
	364.49	81.50
	642.72	7.16
I-132	522.65	15.99

	630.19	13.32
	667.71	98.70
	772.60	75.60
	954.55	17.57
	1398.57	7.01
Te-132	49.72	14.96
	228.16	88.00
I-133	529.87	87.00
	875.33	4.51
Xe-133	81.00	36.90
Xe-135	249.79	90.00
Ba-140	29.97	14.10
	162.66	6.22
	304.85	4.29
	537.26	24.39
La-140	328.76	20.32
	487.02	45.51
	815.77	23.28

	1596.21	95.40
Ce-141	145.44	48.40
Ce-144	80.12	1.36
	133.51	11.09
Sm-153	103.18	29.25
Ho-166	80.58	6.57
Tm-170	84.25	2.48
Ta-182	67.75	42.92
	100.11	14.20
	152.43	7.02
	222.11	7.57
	229.32	3.64
	264.07	3.61
	1121.29	35.24
	1189.04	16.49
	1221.40	27.23
	1231.00	11.61
W-187	72.00	13.55

	134.25	10.36
	479.53	26.59
	551.55	6.14
	618.37	7.57
	685.81	33.20
	772.87	5.02
Pa-233	311.90	38.50
Np-239	106.12	25.34
	228.18	10.73
	277.60	14.51

A.3 Long-Lived Library

Nuclide	Energy (keV)	Branching Ratio (%)
Sc-46	889.23	99.98
	1120.55	99.99
Cr-51	320.08	9.91
Mn-54	834.85	99.98
Co-58	810.76	99.45
Fe-59	192.34	3.08
	1099.24	56.50
	1291.59	43.20
Co-60	1173.23	99.85
	1332.49	99.98

Zn-69m	438.63	94.88
Rb-86	1077.00	8.64
Sr-90	546.00	100.00
Nb-95	765.80	99.81
Zr-95	724.19	44.27
	756.72	54.38
Mo-99	181.07	6.03
	739.50	12.26
	777.92	4.30
Tc-99m	140.51	89.00
Ru-103	497.08	91.00
	610.33	5.76
In-115m	336.24	48.19
Sb-122	564.24	72.42
I-131	284.30	6.12
	364.49	81.50
	642.72	7.16
I-132	522.65	15.99
	630.19	13.32
	667.71	98.70
	772.60	75.60
	954.55	17.57
	1398.57	7.01
Te-132	49.72	14.96
	228.16	88.00
Xe-133	81.00	36.90
Cs-134	569.33	15.37
	604.72	97.62
	795.86	85.46
Ba-140	29.97	14.10

	162.66	6.22
Ba-140	304.85	4.29
	537.26	24.39
La-140	328.76	20.32
	487.02	45.51
	815.77	23.28
	1596.2	95.40
Ce-141	145.4	48.40
Ce-144	80.12	1.36
	133.51	11.09
Nd-147	91.11	28.08
	531.02	13.37
Eu-152	121.78	39.58
	244.70	10.47
	344.28	95.24
	778.90	46.31
	964.06	20.13
	1085.84	14.03
	1112.08	18.97
	1408.01	28.95
Sm-153	103.18	29.25
Hf-181	133.02	43.31
	345.93	15.12
	482.18	80.50
Ta-182	67.75	42.92
	100.11	14.20
	152.43	7.02
	222.11	7.57
	229.32	3.64
	264.07	3.61

	1121.29	35.24
	1189.04	16.49
	1221.40	27.23
	1231.00	11.61
Hg-203	279.20	81.56
Bi-214	609.32	45.50
	1120.29	14.92
	1238.12	5.84
	1764.49	15.30
Pa-231	27.36	10.45
Pa-233	311.90	38.50
Pa-234	131.30	18.90
	152.71	6.26
	226.50	4.43
	227.25	6.05
	880.50	6.48
	883.24	10.04
	925.00	8.21
	926.72	7.56
	946.00	14.04
U-238	49.55	0.06
	113.50	0.01
Np-239	106.12	25.34
	209.75	3.36
	228.18	10.73
	277.60	14.51
Am-241	26.34	2.27
	59.54	35.90

APPENDIX B. MCNP INPUT FILES

B.1 Material Input File Trial 1

```
1-  HPGe Detector Efficiency
2-  c Trial 1
3-  c coaxial hole in germanium
4-  1 0 (16 -30 -1):(-16 17 -1)
5-  c boron contact
6-  2 23 -2.35 (16 -30 -2 1)
7-  c germanium active region
8-  3 14 -5.323 (-29 15 -3 2):(-14 30 -3)
9-  c germanium dead layer
10-  4 14 -5.323 (-13 14 -4):(-14 15 -4 3)
11-  c aluminum mounting cup
12-  5 13 -2.6989 (-33 16 -5 32):(-16 17 -5 1)
13-  c void space between mounting cup and aluminum cap
14-  6 0 (-33 17 -6 5):(-17 10 -6):(-9 33 -6)
15-  c aluminum cap
16-  7 13 -2.6989 (-9 10 -7 6):(9 -8 -7):(-10 11 -7)
17-  c lithium contact
18-  8 24 -0.534 (-13 16 -32 4):(13 -33 -32)
19-  c source vial lid
20-  9 26 -0.93 (-20 21 -22):(-22 23 -21 24)
21-  c inside of vial
22-  10 27 -1.065 25 -27 -18
23-  c source vial body
24-  11 26 -0.93 (-27 25 -19 18):(-24 27 -19 23):(26 -25 -19)
25-  c inside world with importance
26-  12 6 -0.0012 -28 #1 #2 #3 #4 #5 #6 #7 #8 #9 #10 #11
```

```
c outside world with no importance
13 0 28

1 cz 0.4999 $ germanium hole radius (cm)
2 cz 0.5 $ boron contact outer radius (cm)
3 cz 2.715 $ active germanium outer radius (cm)
4 cz 2.975 $ inactive germanium radius outer (cm)
5 cz 3.125 $ aluminum cup (crystal housing) outer radius (cm)
6 cz 3.7 $ vaccumm gap outer radius/inner cap radius (cm)
7 cz 3.8 $ aluminum cap outer radius (cm)
8 pz 10.725 $ outer top of Al cap (upper boundary of detector)
9 pz 10.625 $ inner top of Al cap
10 pz -10.725 $ bottom of Al cap (inner)
11 pz -13.725 $ bottom of Al cap mounting (outer)
c 12 pz 10.375 $ top of Al housing cup
13 pz 10.175 $ top of Ge dead layer
14 pz 10.075 $ top of active Ge crystal
15 pz 4.275 $ bottom of active Ge crystal
16 pz 4.2749 $ bottom of dead layer and Au contact
17 pz 3.775 $ bottom of Al housing mounting cup
18 cz 1.14 $ type 2 vial body inner radius
19 cz 1.34 $ type 2 vial body outer radius
20 pz 27.430 $ type 2 lid top outside
21 pz 27.130 $ type 2 lid top inside
22 cz 1.27 $ type 2 lid outer radius
23 cz 0.97 $ type 2 lid inner radius
24 pz 26.280 $ type 2 body top outer
25 pz 21.280 $ type 2 body inner bottom
26 pz 21.080 $ type 2 body outer bottom
27 pz 26.080 $ type 2 body top inner
```

```
28 so 100 $ world
29 pz 8.975 $ top of B contact
30 pz 8.9749 $ top of crystal hole
31 pz 22.480 $ type 2 top of solution
32 cz 3.025 $ lithium contact outer radius (cm)
33 pz 10.225 $ top of lithium contact

MODE P
c m22 7000. 0.78084 $filter material
c 8000. 0.209476 18000. 0.009684
m23 5000. 1 $boron
m24 3000. 1 $lithium
m6 7000. 0.7 8000. 0.3 $Air
m13 13000. 1 $Aluminum
m14 32000. 1 $germanium
c m20 82000. 1 $Lead
c m25 79000. 1 $Gold
m26 1000. 0.666667 6000. 0.333333 $Polyethylene
m27 1000. 0.5 17000. 0.5 $ Hydrochloric acid solution
IMP:P 1 1 1 1 1 1 1 1 1 1 1 0
SDEF ERG=D1 CEL=10 POS=0 0 21.88 RAD=D2 AXS=0 0 90 EXT=D3 PAR=2
SC1 Type2 Comb Am241, Cd109, Co57, Ce139, Hg203, Sn113, Sr85, Cs137, Y88, Co60
SI1 L .05954 .08803 .12210 .1659 .2792 .3917 .5140 .6616 .8980 1.173 1.333 1.836
SP1 .0336 .0194 .0181 .0215 .0584 .0630 .1183 .0764 .1869 .1034 .1035 .1976
SI2 0 1.14
SP2 -21 1
SI3 0.6
SP3 -21 0
F8:P 3
E8 0 0.0155 8192I 2.899 $peak resolution 0.35keV/channel
```

87- PHYS:P 100 1 1 $gpe, no e-, coherent scattering

88- NPS 100000000

B.2 Material Input File Trial 2

1- HPGe Detector Efficiency

2- c Trial 2

3- c coaxial hole in germanium

4- 1 0 (16 -30 -1):(-16 17 -1)

5- c boron contact

6- 2 23 -2.35 (16 -30 -2 1)

7- c germanium active region

8- 3 14 -5.323 (-29 15 -3 2):(-14 30 -3)

9- c germanium dead layer

10- 4 14 -5.323 (-13 14 -4):(-14 15 -4 3)

11- c aluminum mounting cup

12- 5 13 -2.6989 (-33 16 -5 32):(-16 17 -5 1)

13- c void space between mounting cup and aluminum cap

14- 6 0 (-33 17 -6 5):(-17 10 -6):(-9 33 -6)

15- c aluminum cap

16- 7 13 -2.6989 (-9 10 -7 6):(9 -8 -7):(-10 11 -7)

17- c lithium contact

18- 8 24 -0.534 (-13 16 -32 4):(13 -33 -32)

19- c source vial lid

20- 9 26 -0.93 (-20 21 -22):(-22 23 -21 24)

21- c inside of vial

22- 10 27 -1.065 25 -27 -18

23- c source vial body

24- 11 26 -0.93 (-27 25 -19 18):(-24 27 -19 23):(26 -25 -19)

25- c inside world with importance

```
26-     12 6 -0.0012 -28 #1 #2 #3 #4 #5 #6 #7 #8 #9 #10 #11
27-     c outside world with no importance
28-     13 0 28
29-
30-     1 cz 0.4999 $ germanium hole radius (cm)
31-     2 cz 0.5 $ boron contact outer radius (cm)
32-     3 cz 2.715 $ active germanium outer radius (cm)
33-     4 cz 2.975 $ inactive germanium radius outer (cm)
34-     5 cz 3.125 $ aluminum cup (crystal housing) outer radius (cm)
35-     6 cz 3.7 $ vacuum gap outer radius/inner cap radius (cm)
36-     7 cz 3.8 $ aluminum cap outer radius (cm)
37-     8 pz 10.725 $ outer top of Al cap (upper boundary of detector)
38-     9 pz 10.625 $ inner top of Al cap
39-     10 pz -10.725 $ bottom of Al cap (inner)
40-     11 pz -13.725 $ bottom of Al cap mounting (outer)
41-     c 12 pz 10.375 $ top of Al housing cup
42-     13 pz 10.175 $ top of Ge dead layer
43-     14 pz 10.075 $ top of active Ge crystal
44-     15 pz 4.275 $ bottom of active Ge crystal
45-     16 pz 4.2749 $ bottom of dead layer and Au contact
46-     17 pz 3.775 $ bottom of Al housing mounting cup
47-     18 cz 1.14 $ type 2 vial body inner radius
48-     19 cz 1.34 $ type 2 vial body outer radius
49-     20 pz 27.430 $ type 2 lid top outside
50-     21 pz 27.130 $ type 2 lid top inside
51-     22 cz 1.27 $ type 2 lid outer radius
52-     23 cz 0.97 $ type 2 lid inner radius
53-     24 pz 26.280 $ type 2 body top outer
54-     25 pz 21.280 $ type 2 body inner bottom
55-     26 pz 21.080 $ type 2 body outer bottom
```

```
27 pz 26.080 $ type 2 body top inner
28 so 100 $ world
29 pz 8.975 $ top of B contact
30 pz 8.9749 $ top of crystal hole
31 pz 22.480 $ type 2 top of solution
32 cz 3.025 $ lithium contact outer radius (cm)
33 pz 10.225 $ top of lithium contact

MODE P
c m22 7000. 0.78084 $filter material
c 8000. 0.209476 18000. 0.009684
m23 5000. 1 $boron
m24 3000. 1 $lithium
m6 7000. 0.7 8000. 0.3 $Air
m13 13000. 1 $Aluminum
m14 32000. 1 $germanium
c m20 82000. 1 $Lead
c m25 79000. 1 $Gold
m26 1000. 0.666667 6000. 0.333333 $Polyethylene
m27 1000. 0.5 17000. 0.5 $ Hydrochloric acid solution
IMP:P 1 1 1 1 1 1 1 1 1 1 1 0
SDEF ERG=D1 CEL=10 POS=0 0 21.88 RAD=D2 AXS=0 0 90 EXT=D3 PAR=2
SC1 Type2 Comb Am241, Cd109, Co57, Ce139, Hg203, Sn113, Sr85, Cs137, Y88, Co60
SI1 L .05954 .08803 .12210 .1659 .2792 .3917 .5140 .6616 .8980 1.173 1.333 1.836
SP1 .0336 .0194 .0181 .0215 .0584 .0630 .1183 .0764 .1869 .1034 .1035 .1976
SI2 0 1.14
SP2 -21 1
SI3 0.6
SP3 -21 0
F8:P 3
```

86- FT8 GEB 7.23e-4 6.84e-4 1.31 $FWHM of energy broadening

87- E8 0 0.0155 8192I 2.899 $peak resolution 0.35keV/channel

88- PHYS:P 100 1 1 $gpe, no e-, coherent scattering

89- NPS 100000000

B.3 Carbon Input File Trial 1

1- HPGe Detector Efficiency

2- c Carbon Trial 1

3- c coaxial hole in germanium

4- 1 0 (16 -30 -1):(-16 17 -1)

5- c boron contact

6- 2 23 -2.35 (16 -30 -2 1)

7- c germanium active region

8- 3 14 -5.323 (-29 15 -3 2):(-14 30 -3)

9- c germanium dead layer

10- 4 14 -5.323 (-13 14 -4):(-14 15 -4 3)

11- c aluminum mounting cup

12- 5 13 -2.6989 (-33 16 -5 32):(-16 17 -5 1)

13- c void space between mounting cup and aluminum cap

14- 6 0 (-33 17 -6 5):(-17 10 -6):(-9 33 -6)

15- c aluminum cap

16- 7 13 -2.6989 (-9 10 -7 6):(9 -8 -7):(-10 11 -7)

17- c lithium contact

18- 8 24 -0.534 (-13 16 -32 4):(13 -33 -32)

19- c source vial lid

20- 9 26 -0.93 (-20 21 -22):(-22 23 -21 24)

21- c inside of vial

22- 10 27 -7 25 -27 -18

23- c source vial body

```
11 26 -0.93 (-27 25 -19 18):(-24 27 -19 23):(26 -25 -19)
c inside world with importance
12 6 -0.0012 -28 #1 #2 #3 #4 #5 #6 #7 #8 #9 #10 #11
c outside world with no importance
13 0 28

1 cz 0.4999 $ germanium hole radius (cm)
2 cz 0.5 $ boron contact outer radius (cm)
3 cz 2.715 $ active germanium outer radius (cm)
4 cz 2.975 $ inactive germanium radius outer (cm)
5 cz 3.125 $ aluminum cup (crystal housing) outer radius (cm)
6 cz 3.7 $ vacuum gap outer radius/inner cap radius (cm)
7 cz 3.8 $ aluminum cap outer radius (cm)
8 pz 10.725 $ outer top of Al cap (upper boundary of detector)
9 pz 10.625 $ inner top of Al cap
10 pz -10.725 $ bottom of Al cap (inner)
11 pz -13.725 $ bottom of Al cap mounting (outer)
c 12 pz 10.375 $ top of Al housing cup
13 pz 10.175 $ top of Ge dead layer
14 pz 10.075 $ top of active Ge crystal
15 pz 4.275 $ bottom of active Ge crystal
16 pz 4.2749 $ bottom of dead layer and Au contact
17 pz 3.775 $ bottom of Al housing mounting cup
18 cz 1.14 $ type 2 vial body inner radius
19 cz 1.34 $ type 2 vial body outer radius
20 pz 27.430 $ type 2 lid top outside
21 pz 27.130 $ type 2 lid top inside
22 cz 1.27 $ type 2 lid outer radius
23 cz 0.97 $ type 2 lid inner radius
24 pz 26.280 $ type 2 body top outer
```

```
25 pz 21.280 $ type 2 body inner bottom
26 pz 21.080 $ type 2 body outer bottom
27 pz 26.080 $ type 2 body top inner
28 so 100 $ world
29 pz 8.975 $ top of B contact
30 pz 8.9749 $ top of crystal hole
31 pz 22.480 $ type 2 top of solution
32 cz 3.025 $ lithium contact outer radius (cm)
33 pz 10.225 $ top of lithium contact

MODE P
c m22 7000. 0.78084 $filter material
c 8000. 0.209476 18000. 0.009684
m23 5000. 1 $boron
m24 3000. 1 $lithium
m6 7000. 0.7 8000. 0.3 $Air
m13 13000. 1 $Aluminum
m14 32000. 1 $germanium
c m20 82000. 1 $Lead
c m25 79000. 1 $Gold
m26 1000. 0.666667 6000. 0.333333 $Polyethylene
m27 6000. 1.0 $ Carbon
IMP:P 1 1 1 1 1 1 1 1 1 1 1 0
SDEF ERG=D1 CEL=10 POS=0 0 21.88 RAD=D2 AXS=0 0 90 EXT=D3 PAR=2
SC1 Type2 Comb Am241, Cd109, Co57, Ce139, Hg203, Sn113, Sr85, Cs137, Y88, Co60
SI1 L .06775 .072 .10011 .13425 .15243 .22211 .22932 .26407 .47953 .55155
    .61837 .68581 .77287 .84676 1.1213 1.189 1.2214 1.231 1.3686 1.5246
    1.8107 2.1131 2.754
SP1 .08099 .02557 .02680 .01955 .01325 .01428 .00687 .00681 .05018 0.01159
    .01428 .06265 .00947 .18653 .06650 .03112 .05138 .02191 .09434 .03412
```

```
84-         .05074 .02685 .09422
85-      SI2 0 1.14
86-      SP2 -21 1
87-      SI3 0.6
88-      SP3 -21 0
89-      F8:P 3
90-      E8 0 0.0155 8192I 2.899 $peak resolution 0.35keV/channel
91-      PHYS:P 100 1 1 $gpe, no e-, coherent scattering
92-      NPS 100000000
```

B.4 Carbon Input File Trial 2

```
1-    HPGe Detector Efficiency
2-    c Carbon Trial 2
3-    c coaxial hole in germanium
4-    1 0 (16 -30 -1):(-16 17 -1)
5-    c boron contact
6-    2 23 -2.35 (16 -30 -2 1)
7-    c germanium active region
8-    3 14 -5.323 (-29 15 -3 2):(-14 30 -3)
9-    c germanium dead layer
10-   4 14 -5.323 (-13 14 -4):(-14 15 -4 3)
11-   c aluminum mounting cup
12-   5 13 -2.6989 (-33 16 -5 32):(-16 17 -5 1)
13-   c void space between mounting cup and aluminum cap
14-   6 0 (-33 17 -6 5):(-17 10 -6):(-9 33 -6)
15-   c aluminum cap
16-   7 13 -2.6989 (-9 10 -7 6):(9 -8 -7):(-10 11 -7)
17-   c lithium contact
18-   8 24 -0.534 (-13 16 -32 4):(13 -33 -32)
```

```
c source vial lid
9 26 -0.93 (-20 21 -22):(-22 23 -21 24)
c inside of vial
10 27 -7 25 -27 -18
c source vial body
11 26 -0.93 (-27 25 -19 18):(-24 27 -19 23):(26 -25 -19)
c inside world with importance
12 6 -0.0012 -28 #1 #2 #3 #4 #5 #6 #7 #8 #9 #10 #11
c outside world with no importance
13 0 28

1 cz 0.4999 $ germanium hole radius (cm)
2 cz 0.5 $ boron contact outer radius (cm)
3 cz 2.715 $ active germanium outer radius (cm)
4 cz 2.975 $ inactive germanium radius outer (cm)
5 cz 3.125 $ aluminum cup (crystal housing) outer radius (cm)
6 cz 3.7 $ vaccumm gap outer radius/inner cap radius (cm)
7 cz 3.8 $ aluminum cap outer radius (cm)
8 pz 10.725 $ outer top of Al cap (upper boundary of detector)
9 pz 10.625 $ inner top of Al cap
10 pz -10.725 $ bottom of Al cap (inner)
11 pz -13.725 $ bottom of Al cap mounting (outer)
c 12 pz 10.375 $ top of Al housing cup
13 pz 10.175 $ top of Ge dead layer
14 pz 10.075 $ top of active Ge crystal
15 pz 4.275 $ bottom of active Ge crystal
16 pz 4.2749 $ bottom of dead layer and Au contact
17 pz 3.775 $ bottom of Al housing mounting cup
18 cz 1.14 $ type 2 vial body inner radius
19 cz 1.34 $ type 2 vial body outer radius
```

```
20 pz 27.430 $ type 2 lid top outside
21 pz 27.130 $ type 2 lid top inside
22 cz 1.27 $ type 2 lid outer radius
23 cz 0.97 $ type 2 lid inner radius
24 pz 26.280 $ type 2 body top outer
25 pz 21.280 $ type 2 body inner bottom
26 pz 21.080 $ type 2 body outer bottom
27 pz 26.080 $ type 2 body top inner
28 so 100 $ world
29 pz 8.975 $ top of B contact
30 pz 8.9749 $ top of crystal hole
31 pz 22.480 $ type 2 top of solution
32 cz 3.025 $ lithium contact outer radius (cm)
33 pz 10.225 $ top of lithium contact

MODE P
c m22 7000. 0.78084 $filter material
c 8000. 0.209476 18000. 0.009684
m23 5000. 1 $boron
m24 3000. 1 $lithium
m6 7000. 0.7 8000. 0.3 $Air
m13 13000. 1 $Aluminum
m14 32000. 1 $germanium
c m20 82000. 1 $Lead
c m25 79000. 1 $Gold
m26 1000. 0.666667 6000. 0.333333 $Polyethylene
m27 6000. 1.0 $ Carbon
IMP:P 1 1 1 1 1 1 1 1 1 1 1 0
SDEF ERG=D1 CEL=10 POS=0 0 21.88 RAD=D2 AXS=0 0 90 EXT=D3 PAR=2
SC1 Type2 Comb Am241, Cd109, Co57, Ce139, Hg203, Sn113, Sr85, Cs137, Y88, Co60
```

```
79-  SI1 L .61837 .68581 .77287 .84676 1.1213 1.189 1.2214 1.231 1.3686 1.5246
80-  SP1 .1 .1 .1 .1 .1 .1 .1 .1 .1 .1 .1
81-  SI2 0 1.14
82-  SP2 -21 1
83-  SI3 0.6
84-  SP3 -21 0
85-  F8:P 3
86-  E8 0 0.0155 8192I 2.899 $peak resolution 0.35keV/channel
87-  PHYS:P 100 1 1 $gpe, no e-, coherent scattering
88-  NPS 200000000
```

B.5 Carbon Input File Trial 3

```
1-   HPGe Detector Efficiency
2-   c Carbon Trial 3
3-   c coaxial hole in germanium
4-   1 0 (16 -30 -1):(-16 17 -1)
5-   c boron contact
6-   2 23 -2.35 (16 -30 -2 1)
7-   c germanium active region
8-   3 14 -5.323 (-29 15 -3 2):(-14 30 -3)
9-   c germanium dead layer
10-  4 14 -5.323 (-13 14 -4):(-14 15 -4 3)
11-  c aluminum mounting cup
12-  5 13 -2.6989 (-33 16 -5 32):(-16 17 -5 1)
13-  c void space between mounting cup and aluminum cap
14-  6 0 (-33 17 -6 5):(-17 10 -6):(-9 33 -6)
15-  c aluminum cap
16-  7 13 -2.6989 (-9 10 -7 6):(9 -8 -7):(-10 11 -7)
17-  c lithium contact
18-  8 24 -0.534 (-13 16 -32 4):(13 -33 -32)
```

```
19-     c source vial lid
20-     9 26 -0.93 (-20 21 -22):(-22 23 -21 24)
21-     c inside of vial
22-     10 27 -7 25 -27 -18
23-     c source vial body
24-     11 26 -0.93 (-27 25 -19 18):(-24 27 -19 23):(26 -25 -19)
25-     c inside world with importance
26-     12 6 -0.0012 -28 #1 #2 #3 #4 #5 #6 #7 #8 #9 #10 #11
27-     c outside world with no importance
28-     13 0 28
29-
30-     1 cz 0.4999 $ germanium hole radius (cm)
31-     2 cz 0.5 $ boron contact outer radius (cm)
32-     3 cz 2.715 $ active germanium outer radius (cm)
33-     4 cz 2.975 $ inactive germanium radius outer (cm)
34-     5 cz 3.125 $ aluminium cup (crystal housing) outer radius (cm)
35-     6 cz 3.7 $ vacuum gap outer radius/inner cap radius (cm)
36-     7 cz 3.8 $ aluminium cap outer radius (cm)
37-     8 pz 10.725 $ outer top of Al cap (upper boundary of detector)
38-     9 pz 10.625 $ inner top of Al cap
39-     10 pz -10.725 $ bottom of Al cap (inner)
40-     11 pz -13.725 $ bottom of Al cap mounting (outer)
41-     c 12 pz 10.375 $ top of Al housing cup
42-     13 pz 10.175 $ top of Ge dead layer
43-     14 pz 10.075 $ top of active Ge crystal
44-     15 pz 4.275 $ bottom of active Ge crystal
45-     16 pz 4.2749 $ bottom of dead layer and Au contact
46-     17 pz 3.775 $ bottom of Al housing mounting cup
47-     18 cz 1.14 $ type 2 vial body inner radius
48-     19 cz 1.34 $ type 2 vial body outer radius
```

```
20 pz 27.430 $ type 2 lid top outside
21 pz 27.130 $ type 2 lid top inside
22 cz 1.27 $ type 2 lid outer radius
23 cz 0.97 $ type 2 lid inner radius
24 pz 26.280 $ type 2 body top outer
25 pz 21.280 $ type 2 body inner bottom
26 pz 21.080 $ type 2 body outer bottom
27 pz 26.080 $ type 2 body top inner
28 so 100 $ world
29 pz 8.975 $ top of B contact
30 pz 8.9749 $ top of crystal hole
31 pz 22.480 $ type 2 top of solution
32 cz 3.025 $ lithium contact outer radius (cm)
33 pz 10.225 $ top of lithium contact

MODE P
c m22 7000. 0.78084 $filter material
c 8000. 0.209476 18000. 0.009684
m23 5000. 1 $boron
m24 3000. 1 $lithium
m6 7000. 0.7 8000. 0.3 $Air
m13 13000. 1 $Aluminum
m14 32000. 1 $germanium
c m20 82000. 1 $Lead
c m25 79000. 1 $Gold
m26 1000. 0.666667 6000. 0.333333 $Polyethylene
m27 6000. 1.0 $ Carbon
IMP:P 1 1 1 1 1 1 1 1 1 1 1 0
SDEF ERG=D1 CEL=10 POS=0 0 21.88 RAD=D2 AXS=0 0 90 EXT=D3 PAR=2
SC1 Type2 Comb Am241, Cd109, Co57, Ce139, Hg203, Sn113, Sr85, Cs137, Y88, Co60
```

```
79-  SI1 L .05 1.5246 1.81072 2.113092 2.754
80-  SP1 .2 .2 .2 .2 .2
81-  SI2 0 1.14
82-  SP2 -21 1
83-  SI3 0.6
84-  SP3 -21 0
85-  F8:P 3
86-  E8 0 0.0155 8192I 2.899 $peak resolution 0.35keV/channel
87-  PHYS:P 100 1 1 $gpe, no e-, coherent scattering
88-  NPS 500000000
```

B.6 Comparison Data Input File

```
1-  HPGe Detector Efficiency
2-  c Comparison Data
3-  c coaxial hole in germanium
4-  1 0 (16 -30 -1):(-16 17 -1)
5-  c boron contact
6-  2 23 -2.35 (16 -30 -2 1)
7-  c germanium active region
8-  3 14 -5.323 (-29 15 -3 2):(-14 30 -3)
9-  c germanium dead layer
10-  4 14 -5.323 (-13 14 -4):(-14 15 -4 3)
11-  c aluminum mounting cup
12-  5 13 -2.6989 (-33 16 -5 32):(-16 17 -5 1)
13-  c void space between mounting cup and aluminum cap
14-  6 0 (-33 17 -6 5):(-17 10 -6):(-9 33 -6)
15-  c aluminum cap
16-  7 13 -2.6989 (-9 10 -7 6):(9 -8 -7):(-10 11 -7)
17-  c lithium contact
18-  8 24 -0.534 (-13 16 -32 4):(13 -33 -32)
```

```
c source vial lid
9 26 -0.93 (-20 21 -22):(-22 23 -21 24)
c inside of vial
10 27 -7.5 25 -27 -18
c source vial body
11 26 -0.93 (-27 25 -19 18):(-24 27 -19 23):(26 -25 -19)
c inside world with importance
12 6 -0.0012 -28 #1 #2 #3 #4 #5 #6 #7 #8 #9 #10 #11
c outside world with no importance
13 0 28

1 cz 0.4999 $ germanium hole radius (cm)
2 cz 0.5 $ boron contact outer radius (cm)
3 cz 2.715 $ active germanium outer radius (cm)
4 cz 2.975 $ inactive germanium radius outer (cm)
5 cz 3.125 $ aluminum cup (crystal housing) outer radius (cm)
6 cz 3.7 $ vaccumm gap outer radius/inner cap radius (cm)
7 cz 3.8 $ aluminum cap outer radius (cm)
8 pz 10.725 $ outer top of Al cap (upper boundary of detector)
9 pz 10.625 $ inner top of Al cap
10 pz -10.725 $ bottom of Al cap (inner)
11 pz -13.725 $ bottom of Al cap mounting (outer)
c 12 pz 10.375 $ top of Al housing cup
13 pz 10.175 $ top of Ge dead layer
14 pz 10.075 $ top of active Ge crystal
15 pz 4.275 $ bottom of active Ge crystal
16 pz 4.2749 $ bottom of dead layer and Au contact
17 pz 3.775 $ bottom of Al housing mounting cup
18 cz 1.14 $ type 2 vial body inner radius
19 cz 1.34 $ type 2 vial body outer radius
```

```
20 pz 27.430 $ type 2 lid top outside
21 pz 27.130 $ type 2 lid top inside
22 cz 1.27 $ type 2 lid outer radius
23 cz 0.97 $ type 2 lid inner radius
24 pz 26.280 $ type 2 body top outer
25 pz 21.280 $ type 2 body inner bottom
26 pz 21.080 $ type 2 body outer bottom
27 pz 26.080 $ type 2 body top inner
28 so 100 $ world
29 pz 8.975 $ top of B contact
30 pz 8.9749 $ top of crystal hole
31 pz 22.480 $ type 2 top of solution
32 cz 3.025 $ lithium contact outer radius (cm)
33 pz 10.225 $ top of lithium contact

MODE P
c m22 7000. 0.78084 $filter material
c 8000. 0.209476 18000. 0.009684
m23 5000. 1 $boron
m24 3000. 1 $lithium
m6 7000. 0.7 8000. 0.3 $Air
m13 13000. 1 $Aluminum
m14 32000. 1 $germanium
c m20 82000. 1 $Lead
c m25 79000. 1 $Gold
m26 1000. 0.666667 6000. 0.333333 $Polyethylene
m27 6000. 1.0 $ Carbon
IMP:P 1 1 1 1 1 1 1 1 1 1 1 0
SDEF ERG=D1 CEL=10 POS=0 0 21.88 RAD=D2 AXS=0 0 90 EXT=D3 PAR=2
SC1 Type2 Comb Am241, Cd109, Co57, Ce139, Hg203, Sn113, Sr85, Cs137, Y88, Co60
```

```
79-     SI1 L .059 .11 .205 .31 .42 .505 .585 .98 1.3 1.45 1.66
82-     SP1 .18 .08 .08 .08 .08 .08 .08 .08 .08 .1
85-     SI2 0 1.14
86-     SP2 -21 1
87-     SI3 0.6
88-     SP3 -21 0
89-     F8:P 3
90-     E8 0 0.0155 8192I 2.899 $peak resolution 0.35keV/channel
91-     PHYS:P 100 1 1 $gpe, no e-, coherent scattering
92-     NPS 100000000
```

APPENDIX C. SURFACE FIT EQUATIONS

C.1 First surface fit with materials

R^2 is .9563

Equation: -1.832723294584355e+02 9.692386166333838e-01*X 1.126625310452928e+02*Y
-5.050660710471379e-02*X^2 -7.848471030399101e-01*XY -2.597306806858189e+01*Y^2
5.439017970156613e-03*X^3 -1.491520705355470e-02*YX^2 2.036096095403908e-01*XY^2
2.586595636943525e+00*Y^3 -7.622485626417497e-04*YX^3 3.082942976650042e-03*(XY)^2
-1.584908823749233e-02*XY^3 -9.426702250398104e-02*Y^4

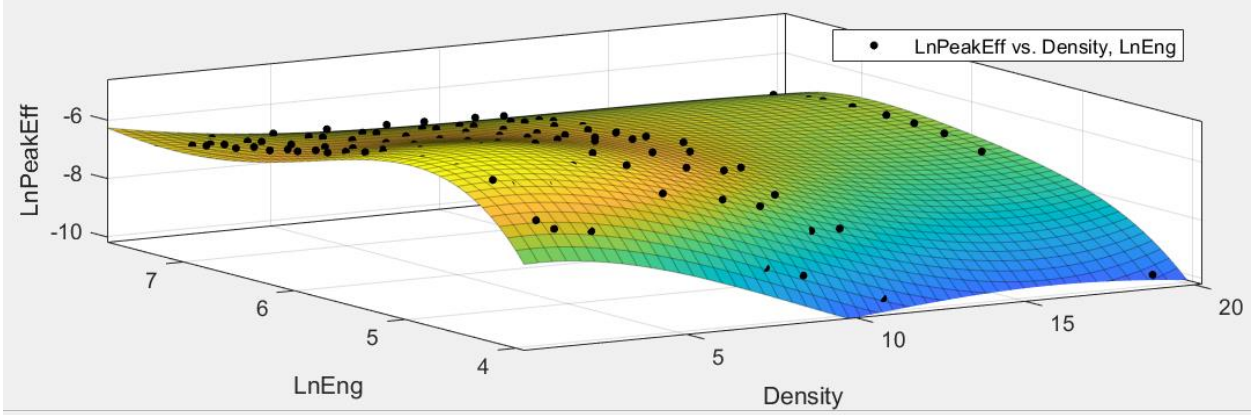

Figure 25: Original Material Surface Fit

C.2 Second surface fit with SPUD materials

R^2=.9611

Equation: -1.117834133639910e+02 3.522769420255257e-01*X 6.610579499612435e+01*Y
-9.928608507177603e-02*X^2 -2.993292059492791e-01*XY -1.483725339008146e+01*Y^2
5.163235462295947e-03*X^3 2.928686645941373e-03*YX^2 9.103079283213690e-02*XY^2
1.428812366533776e+00*Y^3 -7.015559822227540e-04*YX^3 1.435561179776951e-03*(XY)^2
-7.774231095961441e-03*XY^3 -5.019628696040376e-02*Y^4

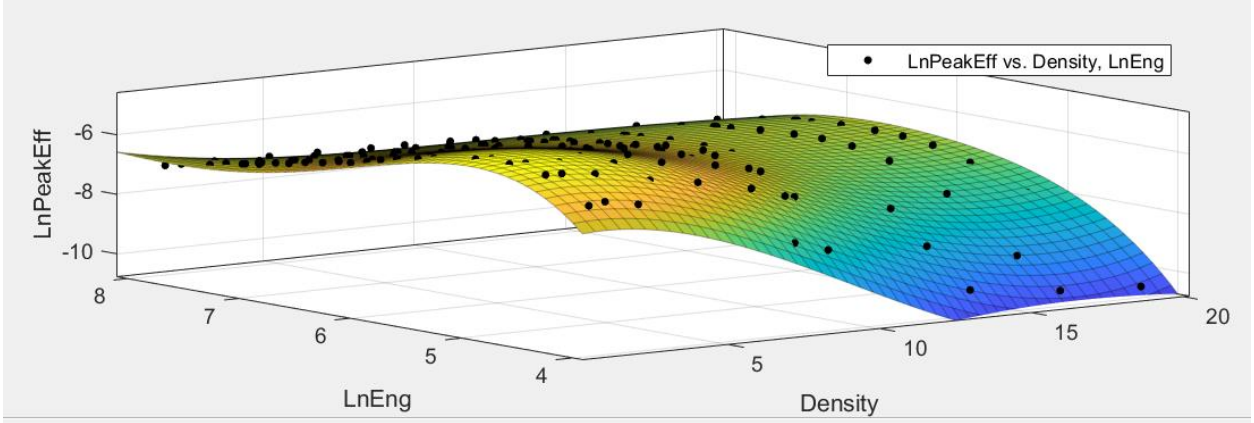

Figure 26: Material Surface Fit with SPUD Energies

C.3 Original Carbon Trial

R^2=.9868

Equation: -1.027733508606305e+02 -7.054372439940557e-02*X 6.279451639537417e+01*Y 5.893843798055446e-03*X^2 -4.236386573663761e-02*XY -1.473334866105163e+01*Y^2 -2.963728768206750e-05*X^3 -1.294170363598505e-03*YX^2 1.164186157481204e-02*XY^2 1.504320105172938e+00*Y^3 4.074452165131946e-06*YX^3 6.959483921653990e-05*(XY)^2 -6.962026989026961e-04*XY^3 -5.711531376601387e-02*Y^4

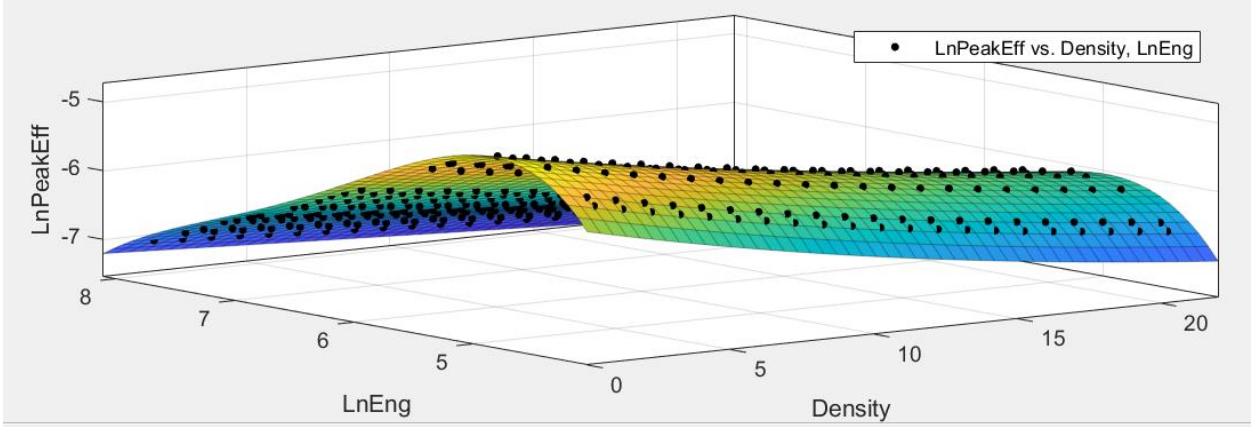

Figure 27: Original Carbon Surface Fit

C.4 Second Carbon Trial With 50 keV

R^2=.9967

Equation: -1.513737317644019e+02 1.929675477897074e+00*X 9.160661335255587e+01*Y 4.883417314446674e-03*X^2 -1.031214371647050e+00*XY -2.095443105233853e+01Y^2 -1.725478733040888e-05*X^3 -1.025862701976635e-03*YX^2 1.715834809403724e-01*XY^2 2.083567685412054e+00*Y^3 2.264186968688332e-06*YX^3 5.223772530711785e-05*(XY)^2 -9.181200775643194e-03*XY^3 -7.668373343555621e-02*Y^4

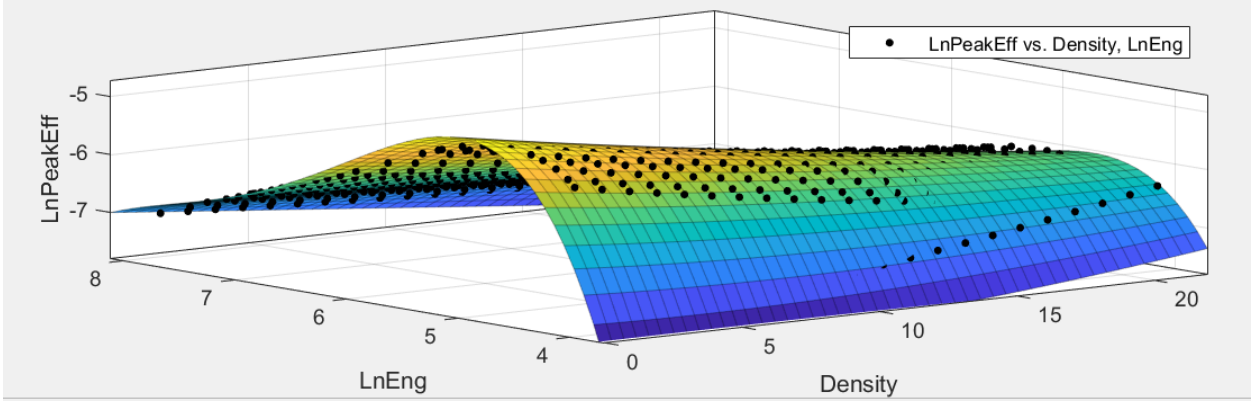

Figure 28: Second Carbon Surface Fit with 50 keV

C.5 Second Carbon Trial Without 50 keV

R^2=.9997

Equation: -1.019219759284939e+02 -1.091508179959940e-01*X 6.227628262250591e+01*Y 5.323283017775840e-03*X^2 -2.046987139391578e-02*XY -1.461942756567664e+01*Y^2 -2.843339093317359e-05*X^3 -1.104401484863275e-03*YX^2 7.647208327974637e-03*XY^2 1.493643180357930e+00*Y^3 3.941005681325931e-06*YX^3 5.408933695550276e-05*(XY)2 -4.605369624591423e-04*XY^3 -5.675659079574896e-02*Y^4

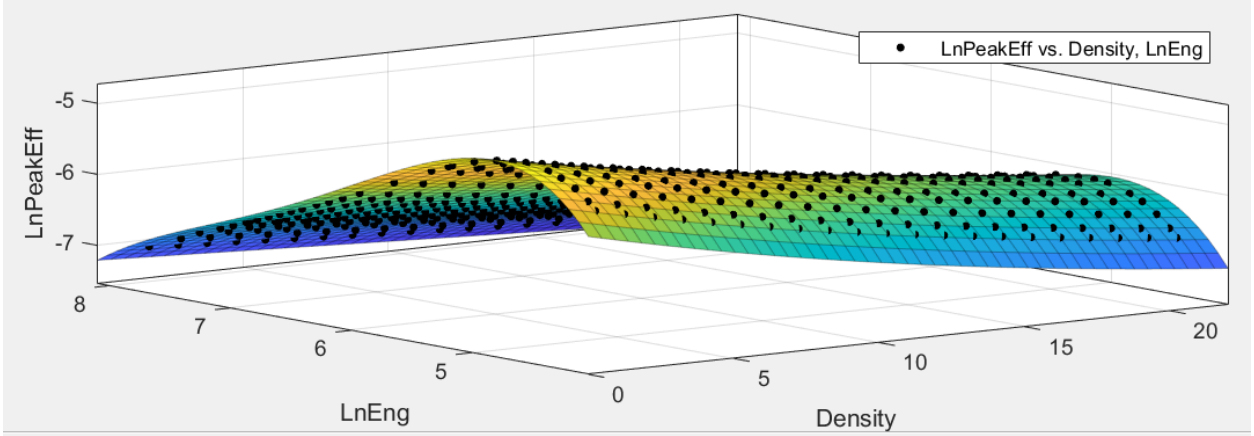

Figure 29: Second Carbon Surface Fit Without 50 keV

C.6 Third Carbon Trial With 50 keV

R^2=.9966

Equation: -1.315042188695590e+02 -1.392306562630849e-01*X 8.213828581025018e+01*Y 5.567101375279870e-03*X^2 -6.484304512266158e-03*XY -1.954483311883006e+01*Y^2 -3.697362708398671e-05*X^3 -1.126707172577356e-03*YX^2 5.436010859503512e-03*XY^2 2.028734183231944e+00*Y^3 5.396817996172993e-06*YX^3 5.103922904080136e-05*(XY)^2 -3.405470592348515e-04*XY^3 -7.826560703778453e-02*Y^4

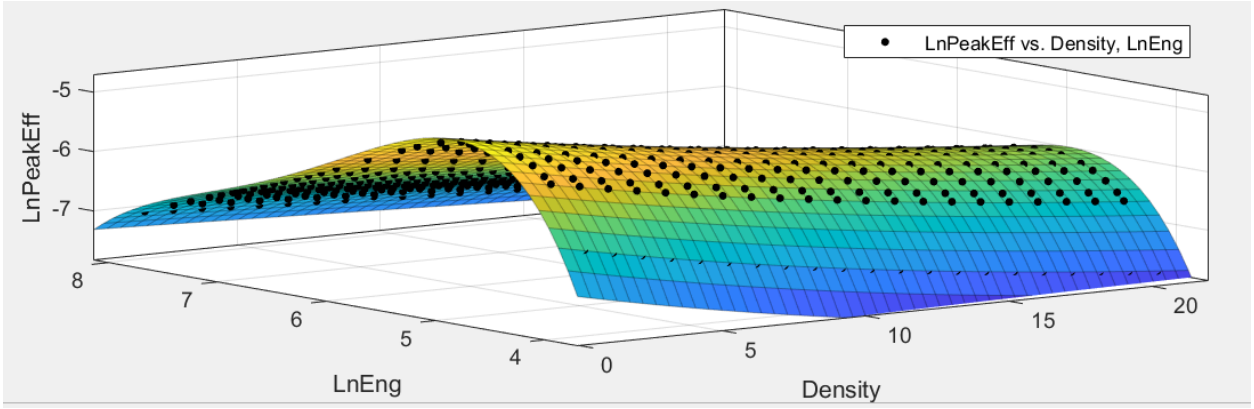

Figure 30: Third Carbon Surface Fit with 50 keV

C.7 Third Carbon Trial without 50 keV

r^2=.9998

Equation: -9.978087091678675e+01 -1.111311024635328e-01*X 6.074133588176213e+01*Y 5.407632967147299e-03*X^2 -1.993454789250648e-02*XY -1.421299488705661e+01*Y^2 -3.326779948668624e-05*X^3 -1.096223698478409e-03*YX^2 7.571829701819151e-03*XY^2 1.446531300906992e+00*Y^3 4.841584514793143e-06*YX^3 5.006874946250347e-05*(XY)^2 -4.530602091909237e-04*XY^3 -5.474034012765846e-02*Y^4

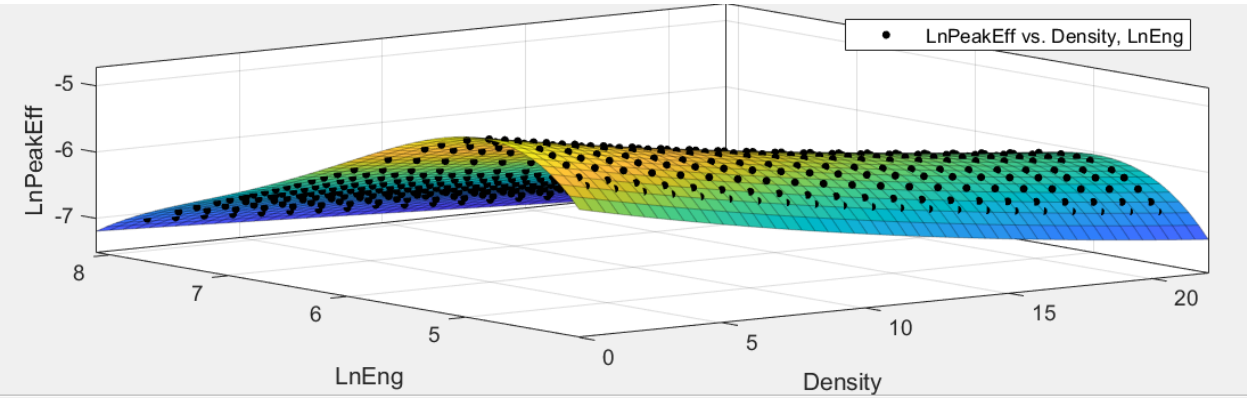

Figure 31: Third Carbon Surface Fit without 50 keV

APPENDIX D. RATIO OF EFFICIENCY CODE

D.1 MATLAB .M File

The following is the MATLAB code to generate a density given ratio of two peak efficiencies In this case the energies are 110 keV and 980 keV and the ratio is 2.643088.

```
%Plug in known energies at unknown Density to get calculated Density
LnEng1=log(120);
LnEng2=log(930);

%Define Components of the Quadratic
p_00=-99.78087091678675;
p_01=60.74133588176213;
p_10=-.1111311024635328;
p_20=0.005407632967147299;
p_02=-14.21299488705661;
p_11=-0.01993454789250648;
p_30=-0.00003326779948668624;
p_21=-0.001096223698478409;
p_12=0.007571829701819151;
p_31=0.00004841584514793143;
p_03=1.44653130090699;
p_22=0.00005006874946250347;
p_13=-0.000530602091909237;
p_04=-0.05474034012765846;

%Ratio of Effs=R
R=2.643088;
```

```
%assuming (ax+bx^2+cx^3+d)/(gx+fx^2+hx^3+k)=ratio of Effs=R
%List all Coefficients
a=p_10+p_11.*LnEng1+p_12.*LnEng1.^2+p_13.*LnEng1.^3;
b=p_20+p_21.*LnEng1+p_22.*LnEng1.^2;
c=p_30+p_31.*LnEng1;
d=p_00+p_01.*LnEng1+p_02.*LnEng1.^2+p_03.*LnEng1.^3+p_04.*LnEng1.^4;

g=p_10+p_11.*LnEng2+p_12.*LnEng2.^2+p_13.*LnEng2.^3;
f=p_20+p_21.*LnEng2+p_22.*LnEng2.^2;
h=p_30+p_31.*LnEng2;
k=p_00+p_01.*LnEng2+p_02.*LnEng2.^2+p_03.*LnEng2.^3+p_04.*LnEng2.^4;

%Defining Coefficients for Quadratic that will be solved to get Density
A=c-h;
B=b-f;
C=a-g;
D=d-k-log(R);

%Write Quadratic and Solve it
J=[A B C D];

Roots_Of_J=roots(J)
```

APPENDIX E. RELATIVE ERROR OF FINAL SURFACE FIT EQUATION

The table on the following page shows the percent error of the surface fit equation for the third carbon trial (without the 50 KeV gamma line). Note that the densities are the half integer values in the first, thirteenth, and twenty-fifth rows, and they in units of grams per cubic centimeter. Also note that the negative values appear in red.

Table 14: Percent Error of Final Surface Fit Equation

Energy (KeV)	1.5	2.5	3.5	4.5	5.5	6.5	7.5
59	8.490101	8.569161	8.608519	8.731877	8.873343	8.8899	9.026544
110	-0.16274	-0.24995	-0.33654	-0.31366	-0.28475	-0.26412	-0.28511
205	0.60374	0.495138	0.451641	0.406531	0.465468	0.500289	0.44405
310	0.919609	0.938906	0.958138	0.85066	0.866655	0.84437	0.830189
420	0.118161	-0.01097	-0.01018	-0.07199	-0.03935	-0.01699	-0.10449
505	0.355029	0.2982	0.379306	0.389737	0.344251	0.3137	0.324716
585	-0.37907	-0.41751	-0.54608	-0.56455	-0.62715	-0.67792	-0.63242
980	-0.50044	-0.4303	-0.39225	-0.28479	-0.30146	-0.29762	-0.12696
1300	1.089168	0.971276	1.019954	1.123091	1.213577	1.181534	1.300033
1450	1.279295	1.270647	1.211345	1.254064	1.183894	1.232673	1.158582
1660	0.53599	0.567146	0.503784	0.448402	0.433505	0.390384	0.355054
Energy (KeV)	8.5	9.5	10.5	11.5	12.5	13.5	14.5
59	9.076173	9.214179	8.934301	9.024664	9.233048	9.292992	9.379293
110	-0.36385	-0.42575	-0.49182	-0.57356	-0.60458	-0.59669	-0.79112
205	0.337573	0.375837	0.252151	0.234531	0.102707	0.03623	0.008702
310	0.818965	0.844981	1.014192	1.064115	1.044617	0.979041	0.781053
420	-0.07795	-0.02512	-0.00187	-0.02808	0.138444	0.19084	0.238412
505	0.441455	0.370459	0.297583	0.289173	0.297225	0.182204	0.035044
585	-0.6187	-0.62738	-0.64477	-0.64132	-0.62198	-0.53169	-0.51068
980	-0.11491	-0.04904	-0.05622	-0.13033	-0.13169	-0.11241	-0.19872
1300	1.358123	1.349312	1.273212	1.191848	1.117237	1.142867	1.232981
1450	1.2023	1.277867	1.307838	1.215649	1.179096	1.223763	1.334251
1660	0.437601	0.534199	0.521299	0.557905	0.536763	0.553657	0.542365
Energy (KeV)	15.5	16.5	17.5	18.5	19.5	20.5	21.5
59	10.2533	10.42619	10.60715	10.77224	10.98002	11.07612	11.53967
110	-0.74395	-0.83428	-0.9661	-1.21931	-1.47192	-1.51762	-1.50574
205	0.051034	-0.21691	-0.32447	-0.47041	-0.54858	-0.76735	-1.0152
310	0.731901	0.582042	0.543229	0.480511	0.401289	0.19416	-0.0372
420	0.247834	0.205894	0.241811	0.139589	-0.03603	-0.11817	-0.25147
505	-0.00334	0.007699	0.05599	-0.06882	-0.1689	-0.3066	-0.36475
585	-0.46018	-0.49443	-0.54795	-0.64976	-0.72233	-0.82483	-0.97305
980	0.078806	0.091033	0.1489	0.059673	0.009039	0.033159	0.073806
1300	0.574362	0.564562	0.555524	0.519189	0.566757	0.613334	0.545283
1450	0.687761	0.630982	0.695683	0.640079	0.713718	0.77295	0.784577
1660	0.644996	0.579569	0.513775	0.54963	0.589553	0.533275	0.534441

REFERENCES

Aghara S, Charlton W. *NIM B*, 248(1), 181-190, 2006.

Abdullah K. Fundamentals in Nuclear Physics. University of Duhok. December 2014.

Berlizov A, Introduction to the Gamma Spectrum Generator, 2011

Biegalski S, Kane N, Mann J, Tipping T, Dayman K. "Neutron Activation of NIST Surrogate Post-Detonation Urban Debris (SPUD) SRMs" Journal of Radioanalytical and Nuclear Chemistry (JRNC). October 2018, Volume 318, Issue 1, pp 187-193.

Burnett J, Milbrath B. "Radionuclide observables for the Platte underground nuclear eplosive test on 14 April 1962" Journal of Environmental Radioactivity. August 2016, Volume 164, pp 232-238.

Currie LA, "Limits for qualitative detection and quantification determination". Analytical Chemistry 40(3):587-593; 1968.

Jodłowski P (2016) "A revision factor to the Cutshall self-attenuation correction in 210Pb gamma-spectrometry measurements" Applied Radiation Isotopes. March 2016, Volume 109, pp 566–56.

Knoll GF. "Radiation Detection and Measurement". 4th Edition. New Jersey: John Wiley & Sons, 2010.

Faizan A. "Difference between Conductor Semiconductor and Insulator." ElectricalAcademia.com.

Genie 2000, Gamma Acquisition & Analysis, V3.4.1 2016.

Gilmore G. "Practical Gamma-ray Spectrometry". 2nd Edition. West Sussex England. John Wiley & Sons, 2008.

Glasstone S, Dolan PJ, eds., The Effects of Nuclear Weapons, 3rd. edn. (Washington, D.C.: DOD and DOE, 1977).

Graham J, Landsberger S. Journal of Radioanalytical and Nuclear Chemistry, 291 (2), 503-507, 2012.

Lewis EE, Miller Jr. WF. “Computational Methods of Neutron Transport”. La Grange Park, Illinois. American Nuclear Society Inc. 1993

National Research Council, Committee on Nuclear Forensics. “Nuclear Forensics: A Capability of Risk.” Copyright National Academy of Sciences 2010.

Tretkoff E, Chodos A, Oullette J. “December 1938: Discovery of Nuclear Fission” American Physics Society (APS) News. December 2007, Volume 16, Number 11.

USPHS, 1964. Final Report of Off-site Surveillance for Operation Nougat. September 15, 1961-June 30, 1962. US Public Health Service Off-site Radiological Safety, USA. SWRHL-1R.

Vieira B, Biegalski S, Freitas M, Landsberger S, Journal of Radioanalytical and Nuclear Chemistry, 270(1), 55-62, 2006.